"There is no object so foul that intense light will not make beautiful"

R.W. Emerson, Poet

Contents

Motivation

Laser science is becoming one of the most fascinating areas of investigation lead by scientists at many different centers, universities and R&D industry divisions. Its fascination comes from the broad number of applications, and lasers are firmly established as instruments in Atomic Physics and time-resolved metrology. Especially, in the last 15 years, an extreme improvement in the temporal resolution of physical processes has been developed, and a central role is played by pulsed lasers. What used to be dubbed ultrafast optics, where the time scale is the femtoseconds regime, is now moving into the light-wave electronics field, where even sub-cycle, attosecond time resolution is achieved [1]. Electronic dynamics in atoms and molecules rule the composition, the characteristics and properties of biological and chemical systems and could be seen as a point of investigation shared between different fields of research: electron motion is also a matter of interest for sciences beyond the pure physics approaches and inquires. The time scale of electron motion in atoms and molecules is a few hundred attoseconds, shorter than any pulse of visible light, shorter even than a single electric field period at any optical wavelength. Recently, in several places around the world through different experiments, it has been demonstrated that strong, short laser pulses can control and manipulate electron motion. At this point, extreme ultraviolet (XUV) pulses occurring in tens or hundreds of attoseconds can be produced. Complex technologies and sophisticated systems should be employed in order to increase the efficiency and the stability of these high-power ultrafast lasers needed to create femtosecond pulses ready to interact with the atomic systems and to generate attosecond XUV pulses, in trains or in single bursts. Given the high accuracy needed for the lasers used in such applications, a careful design of the stability of the fundamental optical properties of the ultrafast pulses involved is crucial. In this scenario, it hauls this thesis project, in which the main purpose is aimed at stabilizing the laser system used for experiments in atomic physics on light and matter interaction.

The main features of ultrafast pulses are: the pulse duration and phase, the beam

position and the pulse energy. The aim of this project is to present a suitable and compact way to achieve a fast position and energy stabilization of a high-power femtosecond laser operating with a repetition rate of 1 kHz. It has to be remarked that these instabilities affect each others, in particular: power fluctuations influence phase stabilization and beam pointing fluctuations affect both of them [2–5]. The atomic physics application where the stability of those characteristics mentioned above plays a central role is Single Attosecond Pulse generation. In fact, for this specific physical phenomenon, the phase stability is essential, and since the other two variables affect deeply this equilibrium, a fast feedback control system has been developed for the femtosecond laser system: two controllers for the position stabilization and one controller for the power stabilization.

The laser system involved is composed of several components in order to achieve the high-intensity ultrafast pulses used to run those experiments. In the Attolab of the High-Power Facility, Lund Laser Center (LLC), pulses from a seed oscillator are stretched, amplified and compressed again by a Ti:Sapphire* based Chirped Pulse Amplifier (CPA). More specifically, the pulses pass through a large folded triplet Öffner grating stretcher, a regenerative amplifier and a cryo-cooled multipass amplifier, both pumped by solid-state Nd:YLF† lasers; finally, there is a double-pass multilayer dielectric grating compressor. After this path, the pulse duration is approximately 30 fs with an energy of circa 3 mJ. The pulses are further compressed in the final part of the setup. Here, few-cycle optical pulses are created, and it is this part that is of special interest of this project. Here, a hollow fiber and chirped mirrors are employed to obtain sub-10 fs pulses. The hollow fiber is a a special kind of optical device employed in different applications among laser engineering. It is a one meter long hollow capillary made of fused silica and with an inner diameter of a few hundred μm. In this context, it has been used in a chamber, where a nobel gas is pumped up to a certain pressure, becoming the media of the hollow fiber core. A nonlinear optical effect is produced, *Self-phase Modulation*, and the pulse spectrum is broadened in order to obtain shorter pulses after several reflections on the chirped mirrors. These devices and effects will be briefly described in the present report.

The beam pointing stabilization system has been developed to achieve a better coupling of the laser pulses to the fundamental mode of the hollow fiber, and further to reduce the fluctuations to get better nonlinear effect along the fiber. The power fluctuations are

---

*Titanium-doped sapphire, the most popular active material for fs pulse generation. It is sometimes referred as Ti:Sa.

†Neodymium-doped yttrium lithium fluoride

controlled in order to do not affect this phenomenon in the fiber. Both systems finally improve even the control of the pulse phase, a feature already implemented in the laser setup [6]. Mechanical oscillations atop the optical benches can alter the beam pointing and power stability; they can also introduce phase shifts and affect the nonlinear effect in the hollow fiber. Those oscillations derive from vibrations of the equipment, the lab structures and of the entire building, as well as from micro draughts. In the particular application, the fluctuations induce temporal variations to the energy and the pointing of femtosecond pulses in ultrashort laser systems using CPA [7]. For this reason a description of the possible laser noise sources will be treated in the present thesis.

In the introductive chapter the main atomic physics context within which the stabilized laser source is used as a tool for experimental physicists will be exposed. In the second chapter a description of the nature of laser noise and a brief mathematical representation of ultrafast pulses and their compression is presented. Further, in the third chapter, the control system configuration and the engineering description including all the devices used will be explained. Finally, in the last chapter, the experimental setup specifications, the disposition of the above mentioned devices along with the obtained results are provided, that show the discrete improvement of the femtosecond laser source performances.

Acknowledgments

The achievements of this Master Project have not been possible without the help of several people, among the Atomic Physics Division staff and from outside. First and foremost, I would like to thank my supervisor Thomas Fordell, a source of inspiration and an example of patience, persistency and competence, from who I have learned more than just science.

I am especially thankful to the head of the Attosecond group, Anne l'Huillier, who gave me the opportunity to work in such a brilliant environment. I would like to give my thanks to the entire group; to Miguel Miranda, my first office mate and accomplice, able to teach you something serious as making jokes, Kathrin Klünder and Marko Swoboda, for their help, the moral German support and the coffee breaks during my experience in the division.

Many other people of the Atomic Physics Division gave me dedication and a tremendous amount of "tips and tricks", allowing me to improve the performances and solve many issues related to the device developed. In particular, Guillaume Genoud, who gave me the initiation to the FPGA programming, Mikkel Brydegaard Sörensen and Zuguang Guan for the electronics. I would like also to thank Anders Persson, always well disposed to share his suggestions and his unequalled amount of competence. I am deeply grateful to Sune Svanberg, who introduced me to the fabulous applied physics research performed in Lund and gave me a lot of motivation and inspiration. It is an honor to have been his student. I thank the entire fantastic division, its head and all the members, forming a powerful and successful team, who have embraced me since the beginning.

Many thanks to Professor Akira Suda from RIKEN in Japan, who replied to my requests in an ultrashort time and clearly showed me the way to get the signal processing circuit to do its job. I am also grateful to Matteo Lucchini, PhD student in Politecnico di Milano, for giving me remote assistance to get the hardware to rock!

A real blessing has been my family, who even through problems and troubles, always supported me anyhow and anytime. Without their love, their support and their kindness,

Chapter 1

Introduction

This introductive chapter will describe the main subject of interest for which the stabilization system has been developed. Since the generation of Single Attosecond Pulses relies on high-order harmonic generation in a nonlinear medium, the description of the physical effect (through a semiclassical approach) is presented. A brief description of two of the possible applications follows, i.e., attosecond pulse trains and single attosecond pulses.

1.1 High–order Harmonic generation and the Three–Step Model

First of all, one has to think about the attosecond pulse of light as the result of an interaction between a strong laser field and atomic clouds, specifically, nobel elements in a gas–jet. In particular, it should be kept in mind that in this context, high–order harmonic generation (HHG) permitted an important development in the field of ultrafast optics and lightwave electronics, and it is the key for the SAP and Attosecond Pulse Train (APT) as well. The laser intensity needed to do these types of experiments is around $I \sim 10^{14}$ W/cm^2; the generated light is emitted in the XUV region. Those kinds of *"generator"* laser systems are generally defined as high-power lasers. Focusing these high power optical pulses, even higher intensity than what it is needed for HHG can be achieved, to the point of being comparable with the entire sun light focused on a pinhead [8]. A semiclassical model will be used to describe the different processes involved in attosecond pulses generation.

Exploiting the interaction between a high–intensity laser field having a duration of a few tens of femtoseconds with a gas–jet of a nobel material, it is possible to create a broad radiation spectrum that goes from the near–IR to the XUV region. It is composed of odd harmonics of the central frequency of the source laser, and from these it is possible to generate trains or isolated attosecond pulses. To explain the phenomena a semiclassical

model is described, otherwise known as the three-step model. For an easier and more pictorial description of the model, the microscopical interaction of the laser field with the Single Active Electron (SAE) is taken into account. In this model, only the valence electron is dealt with and all other electrons remain unperturbed [9]. As the name of the model suggests, the process is divided into three important steps, represented in figure 1.1:

- Ionization by the quantum *tunnel*[*] effect;

- Electron drift induced by the Infrared (IR) laser field;

- Recollision.
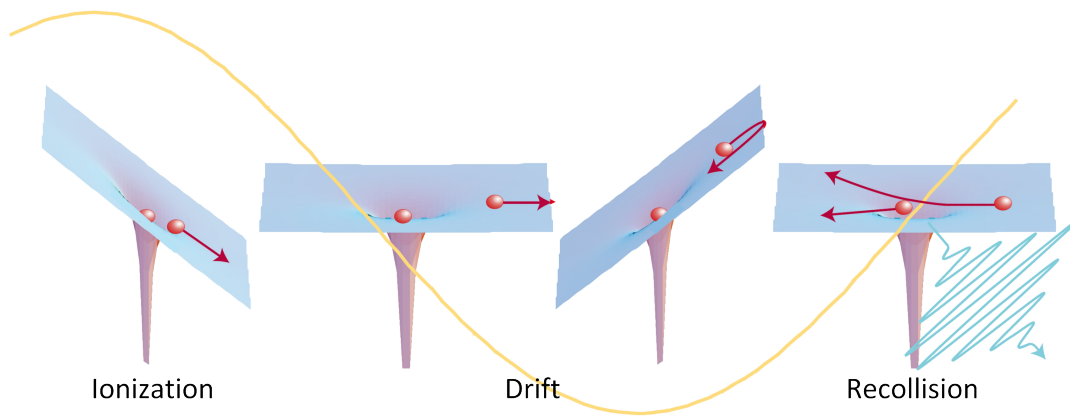
Figure 1.1: A simple scheme of the three-step model.

_____

[*]The tunnel effect is a quantum mechanical phenomenon where an electron, *i.e.* a particle, pass through a potential barrier that it classically could not surmount because its total energy is lower than the potential energy of the barrier.

I STEP: ATOMIC IONIZATION

When the carrier frequency of the laser is lower than the ionization potential, two different situations can take place: multiphoton ionization or tunneling. Which one occurs depends on the value of the *Keldysh parameter* γ, defined as [9]:

$$\gamma = \sqrt{\frac{I_p}{2U_p}},$$

(1.1)

where, in the context of the SAE approximation stated above, the *ionization potential* of the bounded electron is I_p and U_p is the *Ponderomotive energy*, *i.e.*, the cycle avaraged kinetic energy of a free electron in a strong laser E-field:

$$U_p = \frac{e^2 E_0^2}{4m_e\omega_l^2}.$$

(1.2)

When $\gamma >> 1$ the ionization phenomena is treated using lowest order perturbation theory (LOPT). According to this approach an electron can undergo a transition into the continuum from its fundamental state by absorbing n photons, so that

$$n\hbar\omega_l > I_p,$$

where ω_l is the fundamental laser frequency.

The ionization case in the context of HHG is when $\gamma << 1$. In fact the magnitude of the E-field is high and depending on the nobel gases used $10^{13} \leq I_p \leq 10^{15}$ W/cm^2. In this regime the perturbative approach is no longer valid. The electron escapes over the barrier constituted by the sum of the atomic and laser potential into the continuum, as can be seen in figure 1.2.

Specifically, the tunneling probability can be estimated using the ADK theory, named after the physicists M.V. Ammosov, N.B. Delone and V.P. Krǎinov [11]. This theory is characterized by the tunneling time of the electron, which is rapid compared to the oscillation period of the external E-field.
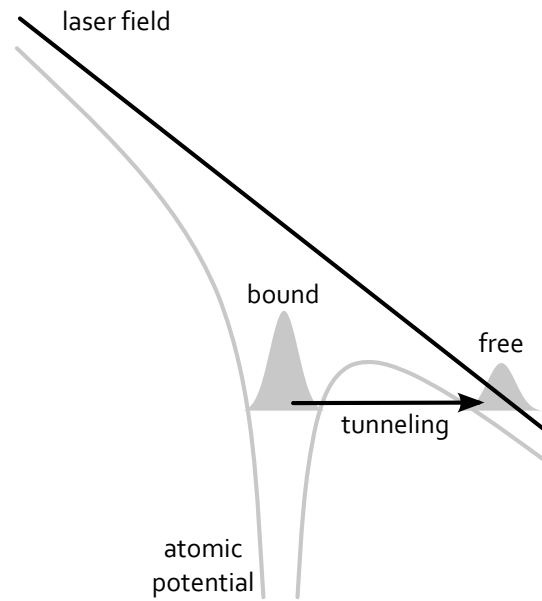
Figure 1.2: The laser field suppresses the binding Coulomb potential so that the electron can escape by tunnel effect. Image from [10].

II STEP: EMITTED ELECTRON MOTION INTO THE IR-FIELD

Once the electron is released into the continuum, the three-step model uses the Newtonian laws and Maxwell equations to model the different possible trajectories of the free electron. Since the electron has tunneled, at time t_i, the kinetic energy increases due to the laser E-field during its acceleration (figure 1.3), assuming a maximum possible value of

$$E_{max} = 3.17 \cdot U_p.$$

For certain values of tunneling time, t_i, the trajectories of the electron cross the origin again, meaning that the electron most likely recombines to the parent ion. In fact, one can show that the kinetic energies are dependent on the phase values of the oscillating electric field. It will be pointed out later the problems related to the phase of the laser pulses once the generation is required with particular characteristics.
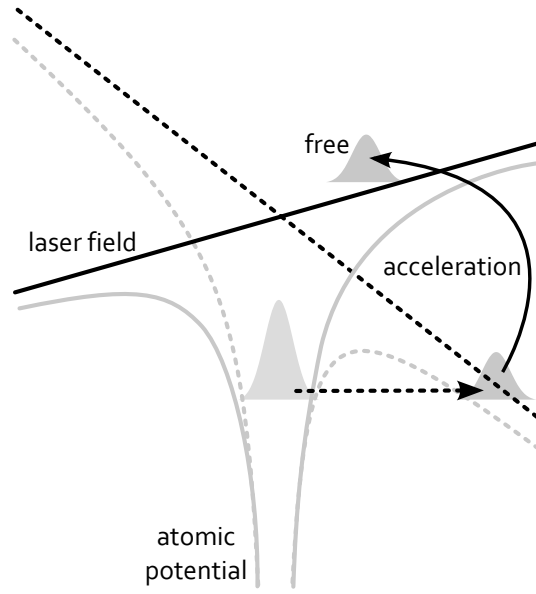
Figure 1.3: Once the electron is in the continuum an increase in its kinetic energy occurs due to the acceleration provided by the strong laser field. Image from [10].

III Step: Radiative recombination

The last step of the generation process is concerned with the emission of the radiation. Once the electron goes back to the parent ion, recombination takes place at the time t_r, and the total energy acquired by the particle in the last step is released as radiative energy, hence an XUV photon is emitted; this process is presented schematically in figure 1.4. Moving toward the parent ion the electron is affected by a sharp deceleration and the energy is released, corresponding to:

$$W_e = K + I_p = \frac{1}{2}mv^2 + I_p, \tag{1.3}$$

where the first term is clearly the kinetic energy acquired by the process during the excursion time $(t_r - t_i)$. When the maximum energy is reached, *i.e.*,

$$K_{max} = \frac{1}{2}mv^2 = 3.17 \cdot U_p, \tag{1.4}$$

the photon emitted is going to have maximum energy, corresponding to the highest frequency of the generated emitted spectra, the so–called *cut–off*:

$$\omega_{cut} = \frac{I_p + 3.17 \cdot U_p}{\hbar}. \tag{1.5}$$
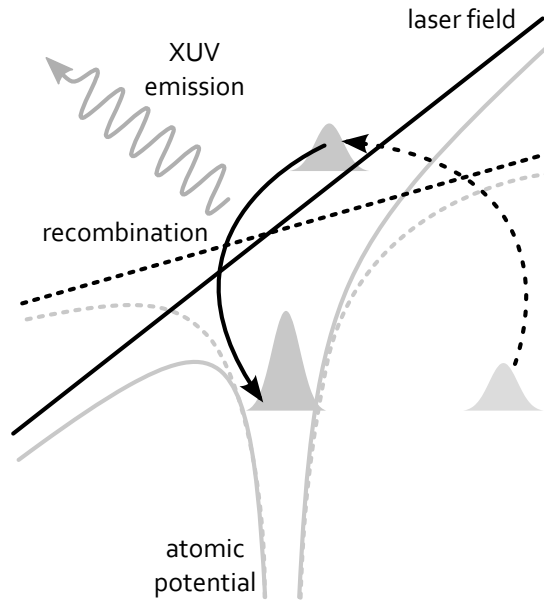
Figure 1.4: The successive collision of the electron with the parent ion undergoes a recombination process and the energy acquired by the electron is released as XUV light. Source: Marko Swoboda, *Attosecond Wave Packet Metrology*, Lund University, 2010.

Since the electron that recombines with the parent ion can have energy between 0 and K_{max}, one expects a continuous spectrum. Actually, this is what happens when a *single* recollision is considered; however, the process is periodically repeated until the fundamental state of the active media is emptied (due to the tunnel effect) producing a discrete spectrum.

The three-step process occurs every half optical cycle, which corresponds to half of the time of the optical period, which for the Ti:Sapphire solid-state laser source corresponds to:

$$T_0/2 = \frac{1}{2} \cdot \frac{2\pi}{\omega_l} = \frac{\pi}{\omega_l} = 2.67/2 \text{ fs} = 1.335 \text{ fs}. \tag{1.6}$$

If one has a 35 fs fundamental laser pulse, it will be expected that greater than 10 cycles are repeated, corresponding to 20 possible emission events (every $T_0/2$). The continua emission for each event then interfere and the inverse of the temporal spacing gives the separation in the frequency domain between the harmonics:

$$\frac{2\pi}{(T_0/2)} = \frac{2\pi}{2\pi/(\omega_l \cdot 2)} = 2 \cdot \omega_l. \tag{1.7}$$

Considering the inversion symmetry felt by the atom every half optical cycle, it is explained why, in the spectrum, one can see only odd orders of the high harmonics. At

the photon energies corresponding to the even harmonic orders, a destructive interference occurs between subsequent half cycles. Breaking the symmetry of the electric fields between two consecutive half cycles, it is possible to achieve the even order harmonic emission, a technique used in two-color HHG [12].

1.2 APT & SAP generation

1.2.1 Attosecond Train of Pulses

The process described above emits, ideally, a sequence of short bursts of radiation every half optical cycle of the femtosecond laser. Seen the considerations given above related to the timings of the different processes giving birth to the high-order harmonics, it is implied that the XUV photon emission happens in a specific time within half an optical cycle and this suggest that as long as the periodicity $T_0/2$ is equal to 1.335 fs the burst of light is therefore well defined and in the attosecond range [13]. Along the several cycles of a relative long IR pulse, the three-step model occurs several times. As presented before, a long pulse ($\sim 35 \text{ fs}$) induces the interference between the generated pulses leading to a spectrum of odd harmonics. This spectrum consists of a series of narrow peaks separated by twice the frequency of the driving field, and it extends far into the XUV regime. It is well established by theoretical studies on the temporal characteristics of the generation process that the HHs are locked in phase. Given the right phase-relation, the sum of these harmonics gives a train of attosecond pulses. Describing the process in the time domain is easier, and the coherent sum of the electric fields of a range of harmonic frequencies (spaced by $2\omega_l$):

$$E_{sum} = \sum_q \left\{ E_q(t) \cdot \exp\left\{ -i\left(q\omega_l t + \varphi_q(\omega) \right) \right\} \right\}, \quad (1.8)$$

where $E_q(t)$ are the harmonics electric field envelopes, ω_l the laser field frequency and $\varphi_q(\omega)$ are the harmonics' spectral phases. The resulting temporal intensity distribution of the APT is $I(t) = |E_{sum}(t)|^2$ with each pulse duration far below the half optical cycle duration as mentioned before. Since in real experiments these pulses are longer and chirped compared to the ideal case, different technics are performed to filter, compress and shape APTs [10, 14, 15] from HHG.

1.2.2 Single Attosecond Pulse generation and the Polarization Gating

To be able to generate an isolated attosecond pulse, what is needed is that the recombination occurs during a single half-cycle of the driving IR field. Due to the short time scales involved, electron's motion in the continuum can only be influenced by the field itself. The recombination process can be controlled if the shape of the laser field can be controlled as well.

The main three methods used to achieve SAPs are:

- Extremely short driving pulses (< 4 fs) combined with High-pass Frequency Filtering of the emitted radiation from the cut-off region;

- Short driving pulses (< 6 fs) combined with Polarization Gating: consists of variation of the polarization of the driving IR pulses;

- Double optical gating: consists of polarization gating combined with the second harmonic of the IR laser.

All of the above methods also require the stabilization of the carrier-to-envelope phase, treated in section 2.6. In the Attolab the technique attempted is the polarization gating combined with few-cycle pulses. The main reason of the device developed for this thesis is to improve the spatial and intensity stabilization in order to achieve a more efficient and controlled pulse compression in the hollow fiber and improve the carrier-to-envelope phase offset stabilization system developed previously for the laser system [6]. Since the most widely used technique is the polarization gating, it can be considered as the most important one for the SAPs generation and it was also the first one exploited in history. Basically, employing the strong dependency of the HHG process to the polarization of the driver field, it is possible to create a window of time (called *gate*) of approximately half of the optical cycle period within which the emission of radiation is high. It has been observed that the efficiency of the HHG is maximum when the driver field polarization is linear and it decreases rapidly as the ellipticity increases. According to the semiclassical description presented before, if the polarization of the generative laser is elliptical, the possible trajectories that the driven electron covers are distorted. This change implies that the probability of recollision to the parent ion decreases. With a suitable modulation of the pulse polarization, it is thus possible to have a spot of time when the ellipticity of the field is really low, hence the HHG process is favored. This time is a fraction of the IR-field pulse. To have a pictorial idea of the process see figure 1.5.
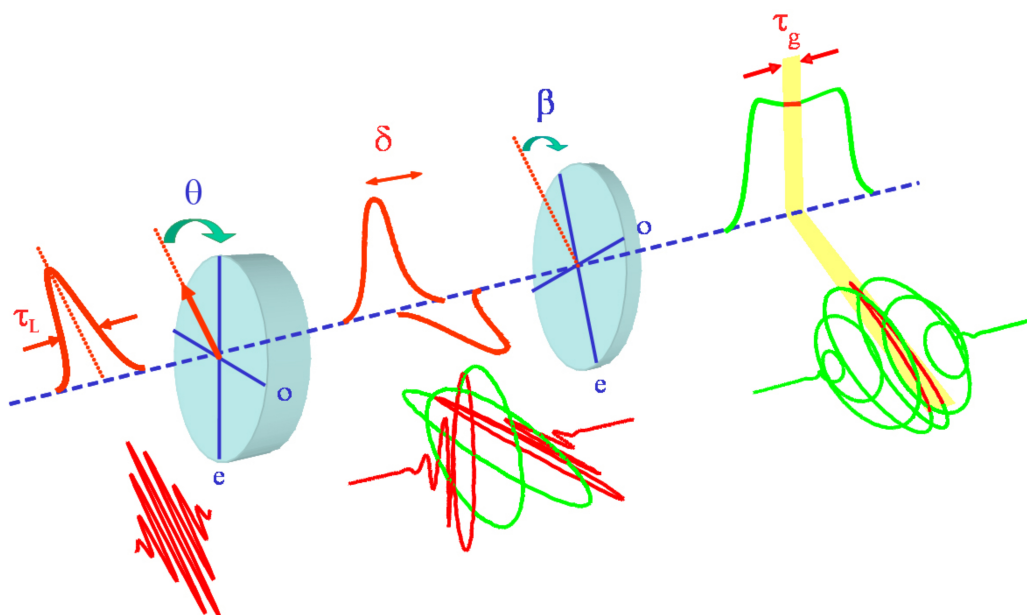
Figure 1.5: Polarization modulation of the input pulse achieved by using two quartz birefrangent plates. The first is thicker in order to introduce a desired delay δ, the second is set as $\lambda/4$ of zero order. Image from [9].

Chapter 2

Laser Noise and Pulse Propagation

This chapter will first introduce and explain the origin of laser beam pointing and power fluctuations, with particular attention to the correctable range of frequencies. These two physical phenomena are two of the three main laser noise components. The third and typically the most interesting, especially in the area of attosecond pulse generation and ultrafast optics, is the carrier-to-envelope phase fluctuation. In particular, this last pulse characteristic and its offset stabilization shall be described. A short descriptions of ultrafast light pulses and their basic characteristics will be analyzed. All of the listed instabilities have different origins, hence, different frequency components, and the importance of the control resides mainly in the long term drifts for the beam pointing (up to several Hz) and in a broader frequency range for the intensity fluctuations. The general origins of these noise effects will be discussed and how and what is affected without a proper compensation.

2.1   Beam Pointing Fluctuations

Beam pointing fluctuations belongs to the group of phenomena that are generally referred to as laser noise, like power and phase noise. This thesis will explain the methods used to stabilize spatial fluctuations and intensity fast variations of the laser beam. The stabilization is predominantly performed to increase the stability of the hollow fiber pulse compressor used to achieve the self-phase modulation, but also to achieve better carrier-to-envelope offset stability; these are concepts that will be treated in this chapter. In terms of beam pointing fluctuations, the uncontrolled directionality for the laser pulses gives problematic issues at the entrance of the fiber. If the beam drifts, the effects are a low coupling efficiency, less broadening of the spectrum, poor beam quality (since higher order modes of the fiber are excited) and possible damage of the fiber entrance. These

beam pointing fluctuations come from, as anticipated, three main different possible effects:

- Mechanical vibrations of the components on the optical benches. These vibrations are also picked up from the ground;

- Thermal effects inducing drifts can affect the alignment of some optical elements;

- Thermal lensing in the gain media along the beam path.

Laser beam alignment can be described by two main parameters: lateral displacement and angular misalignment. The first parameter can be thought of as the x–y offset with respect to the z–axis, the direction of propagation of the laser radiation, which could be continues wave or pulsed. Concerning the angular misalignment, it can be described by the angle swept out by the desired beam propagation axis and the actual one. These two main misalignment problems come from the real world factors highlighted in any kind of laser lab and introduced above. In addition, adjustable mounts used to hold and position lenses along the optical path of the system, mirrors and other components may be affected by the mechanical vibrations, experiencing long term "creep" from stresses and strains which alter the firmness of those optical components. All these issues lead scientists to think about optical realignment to restore the initial accuracy of the beam propagation. Other possible, and definable external factors, may be mechanical shock that occurs when parts are loaded or unloaded to the system and when equipment covers or access doors are opened and shut. The laser in the Attolab at the LLC is a complex and extended system where also a cryo–cooler device is applied to the Ti:Sapphire crystal for the multipass amplification. This is mounted on a separated tripod close to the optical bench, but it is reasonable think that even with this configuration, its vibrations affect the spatial stability of the beam propagation in the area around the stand and even beyond. In situations where these different agents of vibrations exhibit frequencies in resonance with one of the mechanical supports or spring–loaded component mounts, even worse misalignments can occur. Finally, the circulating air turbulence leads to small refractive index changes which affect beam pointing stability [4,7,16].

An additional issue to be pointed out is the influence on the beam pointing fluctuations of others optical devices along the beam. As mentioned before lenses, gratings, beam splitters and any other kind of optical parts are definitely sources of additional vibrations, but another effect occurs: the magnitude and the type of beam pointing fluctuations change

even in an absolutely stable optical components setup. Two following examples can help to obtain a pictorial idea of this important aspect:

- Once the collimated laser beam hits a focusing lens in any position of the entire optical setup the focalized spot of the coming beam will show a transverse random oscillation according to the possible angular misalignment fluctuations. The consequence effect of the lens is to magnify or to shrink (depending which function the lens has) these fluctuations and to change the orientation.

- Another pictorial example is to consider a telescope* for the expansion of the beam size. Placing this optical component at a point on the optical path where the rays are collimated, the resulting effect on the beam is not only the increasing of the beam radius but also the achievement of half the r.m.s.† values.

In the system, different components expand and focus the beam and many lenses are used all along the optical benches, so then in such a complex optical setup, active stabilization is a fundamental aspect to achieve better femtosecond pulsed laser source.

2.2 Power fluctuations

Power fluctuations are an evident expression of what is normally defined as laser *intensity* noise. This aspect should be better described, because fluctuations of beam intensity may be larger than those related to the power. In fact even spatial modes can fluctuate, and then the variable that is changing is the transverse spatial profile. This kind of differentiation is important when many modes are emitted by the source [3]. In the Attolab system, it can be basically considered only one mode propagating, so then the use of both terms is approximately the same.

Laser noise, in general, is an interesting area of research due to the different origins and the many different ways in which the phenomena can be described mathematically and then, practically, to try to avoid them. But technical and mathematical difficulties stand in the way of measuring and quantifying laser noise [2], so it is not always possible to identify with absolute certainty its different components. Noise occurs in all species of lasers and optical cavities for different reasons, and depending on the topology of the

---

*In the compressor of the kHz laser system there is a telescope. Most of the measurements presented with the control system in action were sampled using the piezo-electric mirror as a component of this telescope.

†Root-mean-square

source it is possible to get some core information on the laser itself. For a solid–state laser, which is the main actor in the context of this thesis, the main origins of laser intensity noise are:

- Thermal noise;

- Mechanical vibrations;

- Quantum noise & Amplifier noise.

Thermal noise affects typically all the electronics equipment of the laser system but the temperature changes in the active media result in gain changes, giving power fluctuations. Typically, this generates slow power and pointing drifts. Mechanical vibrations can also give intensity variation effects. As for the beam pointing fluctuations, a proper mounting is important. Even if these first two noise sources are important to be mentioned, their effects are not really deep. Quantum noise with its quantum-mechanical origins and amplifier noise in general can set the limits for laser systems like the one used for this project. These are the two most important contributors of intensity noise.

2.2.1   Quantum noise and amplifier noise

The analysis of electrodynamics and the improvement concerning the studies of the quantum theory of light and matter made possible the birth of what is nowadays labeled as quantum electro-dynamics. In a macroscopic way of thinking, it can be stated that quantum fluctuations affect massively the stability of the photon emission, in fact, different phenomena cause a variability of the photon flux. Quantum noise is normally the limiting factor for the performance of optoelectronic devices and laser sources. Typical effects of quantum noise that can be observed are:

- Shot noise;

- Spontaneous emission of excited atoms or ions;

- Spontaneous Raman Scattering;

- Possible emission from Fluorescence;

- Partition noise generation occurring at each beam splitter;

In the case of a ultrafast laser source the main quantum noise effects are related to spontaneous emission, scattering and relaxation oscillations. The condition that set the uncontrolled photon emission is that the atoms of the active media are excited to a higher-lying energy level. This is certainly the condition required by all the active optical components of the entire laser system. The spontaneous emission occurs when from this higher-lying energy level the electrons fall down into a lower-lying level. This action provides the release of the energy as an emission of a photon which assumes a random direction. To be more specific it should be mentioned that the photon can correspond to any propagation mode of the surrounding cavity of the active medium. Since spontaneous emission is a quantum effect, it is possible to describe it in different ways, using different theories approach. In a semi-classical picture it can be seen as an emission stimulated by the vacuum noise[‡].

The last but not least important of the three main quantum noise contributors is the *relaxation oscillations* (directly descendent from spontaneous emission) which affects the intensity stability of the manipulated beam. In the *"everyday"* use of a femtosecond laser system, when some active components (the main oscillator, the amplifiers or the pumping solid-state and diode lasers) are disturbed during their operations, *e.g.*, by some fluctuations or variations of the laser parameters, their output power does not immediately return to the main steady-state operation but pass through this step of relaxation oscillations [2, 3]. It is, therefore, natural to think that the cumulative effect of all these perturbations gives a random noisy shape to the detected power signal at the final path of the optical beam. It finally makes sense to think that these kinds of quantum effects are particularly relevant in the treatment of laser noise, its analysis, its detection and to design the proper controller system able to stabilize the intensity output.

Amplifier noise is the sum of all those quantum noise components added by the amplifier itself to the main optical beam. This unavoidable excess of noise is generated by all the previously mentioned effects into the gain active media of the Amplifier. It should be specified, that in the laser system of this project, the pulse energy fluctuations are mainly due to the Q-Switched Nd:YLF pump lasers.

[‡]The Vacuum Noise is quantum noise related to the zero-point fluctuations of the electric field in the vacuum state. It is a fairly weak component of the dynamic instabilities but it can affect the properties of the noise and in some extreme case even the function of the optical devices [17].

2.3   Ultrafast high–intensity laser pulses

2.3.1   Pulse description

The stabilized laser system is a pulsed light source, as mentioned before. The pulses of light come as a train with a repetition rate of $1\,\mathrm{kHz}$. The pulses in the setup are created, stretched, amplified, re-compressed to the shortest duration possible. This process is called Chirped Pulse Amplification (CPA) and it will be described later in this chapter. In the following, a brief mathematical description of ultrashort pulses and their main characteristics will be given.
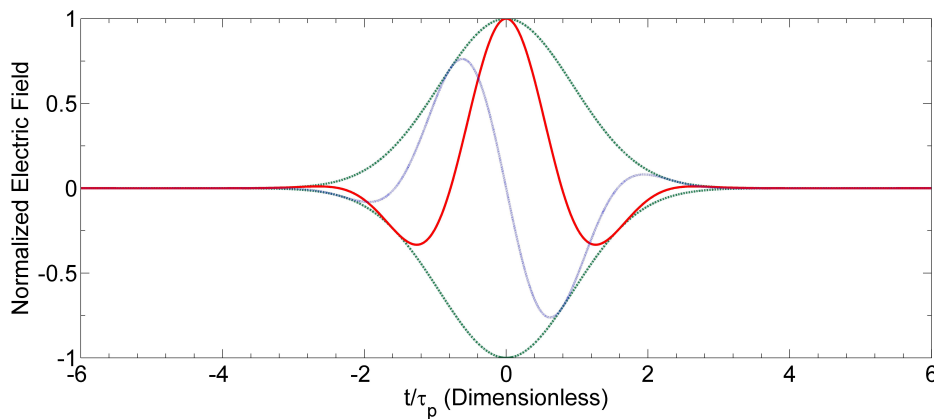

Figure 2.1: Electric field of two consequent extremely short pulses. The first with $\varphi_0 = 0$ (solid red line) and the second with $\varphi_0 = \frac{\pi}{2}$ (dashed line). Around the Electric field oscillation it can be seen the envelope, equal for both pulses. This results is the desired in order to achieve SAP generation, as it will discussed later in this chapter.

Femtosecond laser pulses are electromagnetic wave packets, hence it is possible to describe their electric field mathematically in time and space. Since the approach is governed by a classical treatment, this electric field appears as a solution of the Maxwell wave equation and practically the measured quantities of the pulses are strictly related to the electric field, so it is possible to disclose detected values mathematical expressions [18].

The complex time dependent electric field of a pulse is usually expressed with an amplitude function and a phase term[§]:

$$\tilde{E}(t) = \frac{1}{2}\mathcal{E}(t)e^{i\Gamma(t)}. \tag{2.1}$$

The phase term is a crucial part for the short pulse description. The spectral amplitude of the pulse is centered around a certain mean value ω_l and will have nonzero values in a

---

[§]In this first description the propagation of the pulses is not taken into account, only the single shot temporal characteristics.

range $\Delta\omega$ that is usually smaller compared to the central frequency ω_l. For these reasons it is convenient to introduce the central *carrier frequency* ω_l into the time dependent expression in equation 2.1, rewriting $\Gamma(t)$ as:

$$\Gamma(t) = \varphi_0 + \varphi(t) + \omega_l t. \tag{2.2}$$

So it follows that:

$$\tilde{E}(t) = \frac{1}{2}\mathcal{E}(t)e^{i\varphi_0}e^{i\varphi(t)}e^{i\omega_l t}, \tag{2.3}$$

condensing the real amplitude function with the constant phase term φ_0 and the time-dependent term $\varphi(t)$, yields

$$\tilde{E}(t) = \frac{1}{2}\tilde{\mathcal{E}}(t)e^{i\omega_l t}, \tag{2.4}$$

where $\tilde{\mathcal{E}}(t)$ is the complex field envelope. The phase terms expressed in 2.2 corresponds to a constant phase term φ_0, the time-dependent phase term $\varphi(t)$ and, as stated before, the carrier frequency ω_l. In some cases the constant term of phase can be neglected, but in the sub-10 femtosecond region this is known as the *carrier-to-envelope phase* (CEP) term and it will be characterized by the notation ϕ_{CE}. In figure 2.1 it can be clearly seen the representation of two extremely short pulses superimposed. As it can be noticed the envelope function is exactly the same for the two pulses (the dark green line), but the constant phase term is different. The reader should take into account the following key point: the carrier oscillation of the electric field is fast compared to the slowly varying envelope function of the pulse. This fact sets a limitation since the assumption can be done only for several-cycles optical pulses. In the case of few-cycles or even single-cycle pulses[¶], the two terms of the electric field vary with a comparable speed, hence, different mathematical models are used.

Considering expression 2.5 below, it is now expressed pointing out the carrier angular frequency and the carrier-to-envelope phase, in order to underline the importance of this last term with a change of notation:

$$\tilde{E}_p(t) = \frac{1}{2}\hat{\mathcal{E}}(t)e^{i(\omega_l t + \phi_{ce})}, \tag{2.5}$$

where $\hat{\mathcal{E}}(t) = \mathcal{E}(t) \cdot e^{i\varphi(t)}$ is the envelope function and ϕ_{ce} is the carrier-to-envelope phase. According to the dispersive material having refractive index n within which the pulse propagates, the instantaneous power of the pulse (in Watts) can be expressed as

---

[¶]A single-cycle pulse, the shortest possible waveform at a given wavelength, occurs when the electric field within the envelope of an ultrashort laser pulse performs just one period before the pulse ends, like the one in figure 2.1

the integral of the square of the electric field over the cross section, according to the Poynting theorem of electrodynamics:

$$P(t) = \epsilon_0 cn \int_A dS \frac{1}{T} \int_{t-T/2}^{t+T/2} |\tilde{E}_p|^2(t')dt', \qquad (2.6)$$

considering T as one optical period duration, A the laser beam cross section and obviously c the velocity of light in vacuum. Even with the fastest detectors available today, details of femtosecond pulse envelopes cannot be resolved directly, but only through indirect measurement techniques and the optical period should be substituted by the time response of the detector used. In order to achieve the intensity it is enough to remove the surface integration term, obtaining:

$$\begin{aligned} I(t) &= \epsilon_0 cn \frac{1}{T} \int_{t-T/2}^{t+T/2} |\tilde{E}_p|^2(t')dt' \\ &= \frac{1}{2}\epsilon_0 cn \mathcal{E}^2(t) \\ &= \frac{1}{2}\epsilon_0 cn \tilde{\mathcal{E}}(t)\tilde{\mathcal{E}}^*(t). \end{aligned} \qquad (2.7)$$

The pulse duration τ_p is defined as the full width at the half maximum (FWHM) of the intensity profile, and the spectral width $\Delta\omega_p$ is defined as the FWHM of the spectral intensity $\left|\tilde{\mathcal{E}}(\Omega)\right|^2$, which, in turn, is defined as the Fourier transform of the envelope function introduced in equation 2.4:

$$\begin{aligned} \tilde{\mathcal{E}}(\Omega) &= \int_{-\infty}^{+\infty} \tilde{\mathcal{E}}(t)e^{-i\Omega t}d\Omega \\ &= \int_{-\infty}^{+\infty} 2 \cdot \tilde{E}(t)e^{-i\omega_l t}e^{-i\Omega t}d\Omega \\ &= 2 \cdot \int_{-\infty}^{+\infty} \tilde{E}(t)e^{-i(\Omega+\omega_l)t}d\Omega. \end{aligned} \qquad (2.8)$$

For many different theoretical situations, the pulse shape is described as a predefined mathematical function, such as a Gaussian or a Sech squared profile. In the case of the Gaussian profile, we can write:

$$\tilde{\mathcal{E}}(t) = \tilde{\mathcal{E}}_0 \exp\{-(t/\tau_G)^2\}, \qquad (2.9)$$

and knowing that the FWHM corresponds to $\tilde{\mathcal{E}}(t) = \frac{1}{2}\tilde{\mathcal{E}}_0$, it is immediate the result

$$\tau_G = \frac{\tau_p}{\sqrt{2\ln(2)}}. \qquad (2.10)$$

In respect to the Fourier transform theory, it is well established the connection between the spectral characteristics and temporal characteristics of a function, and this is reflected

as a dependence between the bandwidth $\Delta\omega_p$ and the pulse duration τ_p. This dependence is known as minimum bandwidth-duration product:

$$\Delta\omega_p \cdot \tau_p = 2\pi \cdot \Delta\nu_p \cdot \tau_p \geq 2\pi \cdot c_B, \tag{2.11}$$

where c_B is a constant of the order of 1 and it depends on the pulse shape (Gaussian 0.441, Lorentzian 0.142, Secant 0.315, ect.). The relation is valid as long as the pulses have no frequency modulation. Such pulses are called "bandwidth limited" or *Fourier Transform Limited*. It is easy to check if the frequency is modulated. The instantaneous frequency, obtained by differentiating equation 2.2 is:

$$\frac{d\Gamma(t)}{dt} = \omega_l + \frac{d\varphi(t)}{dt}. \tag{2.12}$$

The criteria to find out the modulation is easy. If the result of the derivation gives a constant as the result, $\frac{d\varphi(t)}{dt} = $ const, the frequency of the pulse is not modulated; otherwise we can have two different cases related to the fact that $\frac{d\varphi(t)}{dt} = f(t) \neq 0$, a condition that results in a *chirped pulse*. The first case is called *up-chirped* pulse, if $\frac{d^2\varphi(t)}{dt^2} > 0$, and the second is called *down-chirped* when $\frac{d^2\varphi(t)}{dt^2} < 0$.

An important concept to point out is that in the case of femtosecond pulses it is difficult to determine with certainty the detailed characteristics of the pulse; therefore, special methods are needed to experimentally determine the pulse shape and characteristics (SPIDER,FROG) [19]. *Autocorrelation* is one of these important methods to obtain a pulse duration estimation, readily accessible through measurements and mathematically corresponding to the convolution of the intensity function 2.7:

$$A_{int}(\tau) = \int_{-\infty}^{+\infty} I(t) \cdot I(t-\tau)dt. \tag{2.13}$$

2.4 Chirped Pulse Amplification: not only ultrafast pulses, but of high power as well

Mode-locked oscillators generate pulses with energies typically on the order of nJ. For 100 fs pulses at 100 MHz repetition rate, this corresponds to peak power of the order of 10 kW. Considering focusing to a spot size of circa λ^2, the intensity value is approximately 10^{12} W/cm^2, which is not enough for HHG and other high–field experiments. This is why amplification is needed to perform experiments in atomic and plasma physics. Femtosecond pulse amplifiers are nowadays able to give energies up to several joules, achieving amplification factors in the range of 10^6 to 10^9. Chirped Pulse Amplification

is a well established technique for picosecond and femtosecond pulse amplification and it revolutionized high-power laser science in terms of focusable beam intensity. The first use of this technique was during World War II in the context of radar systems. Radars are subject to peak power limitations, since the electronics producing the signals of such a high impulsive energy content cannot deal with correct transmissions without component damage and loss of transmitted information. For this reason longer pulses were, and actually are, needed in order to increase the energy while keeping the peak power low, in order to increase the range over which the radar can operate. In any case, the use of longer bandwidth limited pulses degrades the range resolution. Therefore chirped radars are used, and once the radiation scatter back from the object, the received pulse is compressed down to the bandwidth limited value providing high range resolution (in terms of time). During 1985, Donna Strickland and Gerard Mourou presented the adaptation of this system to an optical setup [20], successfully achieving the amplification and the consequent recompression of picosecond pulses. The work at that time consisted of a fiber setup for stretching of low energy pulses, an amplification stage and compression of the high-energy pulses in a double grating compressor. Nowadays laser science is dealing with amplified pulses that reach terawatt and petawatt peak powers (10^{12} W and 10^{15} W respectively) [21, 22].
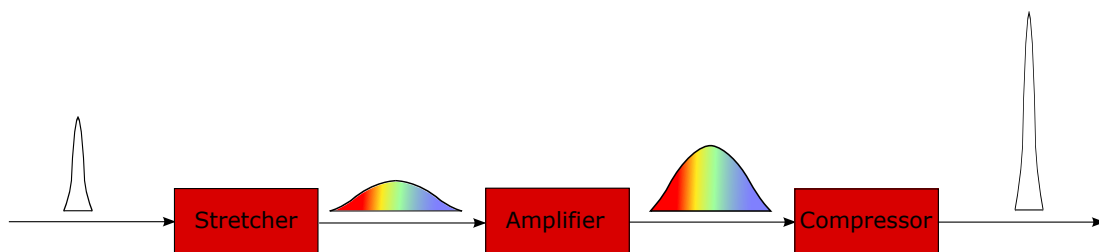

Figure 2.2: Schematic representation of the CPA system concept.

The onset of nonlinear effects such as *self-focusing* related to beam peak power and *multi-photon-ionization* related to beam peak intensity, limit the achievable high energy pulses. Currently the only way to generate strong laser fields able to strongly interact with atomic electron clouds and to generate terawatt and petawatt sources is to exploit the CPA technique. Analyzing the sketch in figure 2.2 we can understand in detail the different parts of the amplification system:

- **Stretching**
  The pulses acquire Group Delay Dispersion(GDD), which lead to highly chirped,

stretched pulses. The GDD is second-order chromatic dispersion, the second deriva-
tive of the spectral phase change. This can be of positive or negative sign. The
stretcher preserves the bandwidth but lowers the peak power according to the
stretching factor, typically 10^3-10^4. In the first experiment, in [20], a single-mode
optical fiber was used, but nowadays systems generally use multilayer optical grat-
ings, presented in section 2.4.1;

- **Amplification**
  The stretched pulses are then amplified. This process can occur in one or multiple
  passages through single- or multiple-stage amplifiers. In accordance to what has
  been declared above, this process occurs without problems of nonlinearities in the
  active media of the amplifier due to the stretching, and without optical damage to
  the crystal itself;

- **Compression**
  Once the pulses achieve the desired energy level, they are sent through a second
  GDD optical line having the opposite sign of the dispersion coefficient with re-
  spect to the stretcher. With proper matching of the two GDDs, the pulses can be
  compressed down to the bandwidth limit.

Figure 2.3: Stretcher.

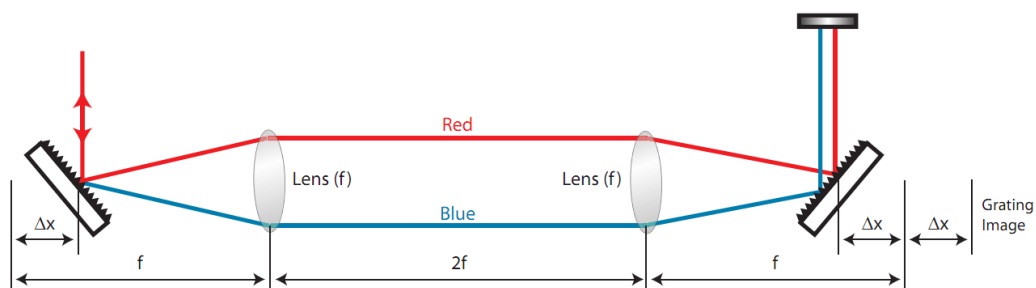## 2.4.1 Multilayer Dielectric Gratings

In grating based stretchers and compressors, multilayer dielectric gratings are often used.
These optical components act in principle as the widely used traditional metallic diffractive
gratings. The principle behind the dispersion is called *angular dispersion*. The central
point is that the gratings reflect the light, diffracting it by the periodic groove structure

into different angles depending on the wavelength. This means that if the incoming beam contains two or more colors, the outgoing angles change for the different wavelengths; hence, a laser beam with a broad spectrum is separated into many–color outgoing beams. In principle this configuration can be applied perfectly in the case of CPA setups, but the limitation is given by the metallic structure of the surfaces. Since the intensities should not overcome the threshold for optical damage, metallic diffractive gratings are a limitation in the production of short and high–energy pulses. For this reason, trans- parent dielectric materials are needed and since they are insulators, they cannot reflect through conductive electrons. The high reflectance properties and the different possible reflectance–wavelength characteristics come from the layered structure of these compo- nents. The multilayer structures consist of alternating layers of high– and low–refractive index materials and achieve high reflectivity through *interference*. In fact, such a structure reflects light by the succession of surfaces whose separations are designed in order to get the desired reflection. This main idea allows optical designers to combine high–reflectivity with high damage thresholds [21–23]. In a typical CPA setup, the stretcher is composed by two gratings, as many as for the compressor; examples of two possible configurations for the two CPA setup components are represented in figures 2.3 and 2.4.

2.5   Further pulse manipulation

2.5.1   Pulse Spectral Broadening

At the output of the CPA system, the pulse duration is of the order of a few tens of femtoseconds, with an energy content of a few millijoules. These numbers are typical in a
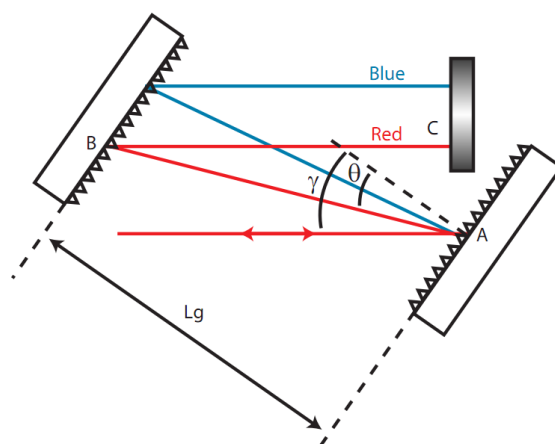

Figure 2.4: Compressor.

setup of ultrafast optics and high-intensity lasers dealing with HHG and attosecond pulse generation. As mentioned in section 1.2.2 on page 8, shorter pulses with high energy are required to generate SAPs without the use of temporal gating techniques (less than $4\,\mathrm{fs}$ are required to avoid the use of temporal gating). In order to do this, fewer cycles are needed, towards the single optical cycle.

In 1996, in the Physics Department of Politecnico di Milano, Mauro Nisoli in the group founded by Orazio Svelto, demonstrated a new technique that can be used to gain additional compression of the pulses without major energy losses of the ultrafast source [21, 24]. That experiment broke through the $10\,\mathrm{fs}$ barrier and opened the doors to a new challenging way to achieve high-energy few-cycles optical pulses. The innovative idea was to implement a hollow fiber instead of a single-mode optical fiber for spectral broadening. The use of a standard single-mode fiber is limited to low energy pulses (nJ) because of two different effects: material damage and high nonlinear optical effects that can degrade the quality of the light pulses [25]. The guided propagation of the pulses enables spectral broadening thanks to *self-phase modulation* (SPM). The temporal compression of picoseconds pulses by SPM in a fiber dates back to 1970, and in the next decade it was developed to be implemented in fibers of different materials and compositions [26]. The hollow fiber instead allows considerably higher energy pulses, up to several mJ. SPM is a third-order optical effect, where the nonlinear polarization oscillation introduces a broadening of the input spectrum in the hollow fiber. New spectral components are generated along the fiber: the red components are generated in the front of the pulse and the blue at the back. Consequentially the temporal matching of the spectral pulse components is needed: in fact, thanks to the spectral broadening new colors out-of-phase are generated, therefore the phase recombination is achieved exploiting chirped mirrors in the Attolab. This dispersion compensation can be achieved in different ways, such as with chirped mirrors, prisms and/or a spatial light modulators [25].

The Hollow Fiber

The hollow fiber, as the name suggests, presents a hole all along the length of the fused silica glass capillary. It is mounted inside a gas-filled tube, right in the middle, with two metal bars keeping the fiber straight, as schematically shown in figure 2.5. The laser beam enters and exits the tube through quartz windows at Brewster angle.

There are two important features to take into account about the use of the hollow

fiber in this application. First of all the nature of the spatial modes propagating along the fiber and their *attenuation*. Then, observing that the better the coupling, the better the light is broadened and propagated, the *coupling efficiency* becomes a crucial factor. This is precisely why the stability of the input laser beam plays a central role, hence, a constrain on the terms of spatial and power fluctuations has to be imposed. Furthermore, without control of the laser beam position, the input capillary portion of the fiber can be damaged. The gases used to fill the chamber are nobel gases and the choice gives several advantages. First, from a pure optical point of view, they exhibit a pure third–order nonlinearity for not exceedingly high pressures. Second, by changing the nobel gas and the pressure inside the chamber, it is possible to control the strength of the nonlinear effect. And last, these gases have a high threshold for multi–photon ionization in terms of intensity; hence, the atomic equilibrium of the gas is not affected and only optical properties are exhibited [24]. A detailed analysis of the properties of the modes has been performed by Marcatili and Shmeltzer [27]. The losses into the fiber along the propagation direction makes a discrimination in favor of the fundamental mode, the EH_{11} hybrid mode, that is expressed in the following. This is the reason why hollow fibers can be in general considered single mode. The equations presented are meant to describe this hybrid mode
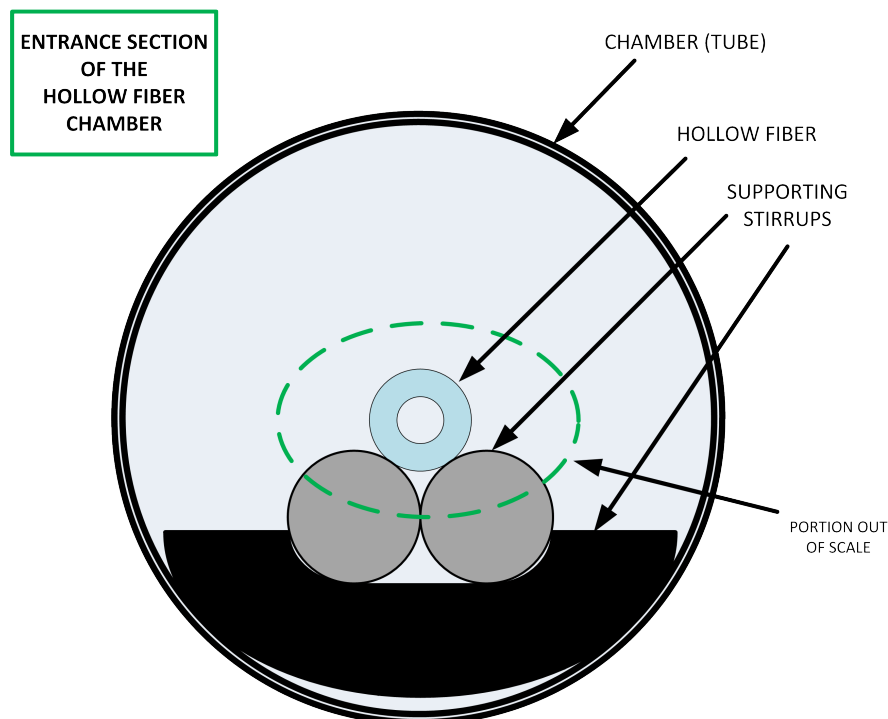

Figure 2.5: Schematic representation of the entrance window of the tubular chamber containing the hollow fiber.

internally in the core. Due to the cylindrical symmetry, the electromagnetic field can be written in the three coordinates θ, r and z:

$$E_{\theta,11} = \left[J_0(k_i r) + \frac{i2.405^2}{2nka} \sqrt{\nu^2 - 1} J_1'(k_i r) \right] \cos(\theta + \theta_0) \exp\{i(\gamma z - \omega t)\} \quad (2.14)$$

$$E_{r,11} = \left[J_0(k_i r) + \frac{i2.405}{2kr} \sqrt{\nu^2 - 1} J_1(k_i r) \right] \sin(\theta + \theta_0) \exp\{i(\gamma z - \omega t)\} \quad (2.15)$$

$$E_{z,11} = -i\frac{2.405}{ka} \cdot J_1(k_i r) \sin(\theta + \theta_0), \quad (2.16)$$

where J_0 and J_1 are the first- and the second-order Bessel functions, n is the refractive index of the internal media, ν is the refractive index of the fiber material, a is the core radius, γ is the axial propagation constant and ω the longitudinal mode frequency. 2.405 is the first zero of the zero-order Bessel function. In equations 2.14, the axial propagation constant γ satisfies the relationship

$$k_i^2 = k^2 - \gamma^2, \quad (2.17)$$

where k_i is the internal radial propagation constant.

The **EH$_{11}$** mode has the smallest losses, and its intensity profile is given by

$$I(r) = I_0 J_0^2 \left(\frac{2.405r}{a} \right). \quad (2.18)$$

The field *attenuation* constant is

$$\alpha = \left(\frac{2.405}{2\pi} \right)^2 \frac{\lambda^2}{2a^3} \, \text{Re}\left\{ \frac{\zeta^2 + 1}{\sqrt{\zeta^2 - 1}} \right\}, \quad (2.19)$$

where ζ is the ratio between the refractive indexes of the external (fused silica) and internal (nobel gas) medium [27]. The coupling between the Gaussian laser mode (it is sufficient to consider only the fundamental mode) and the hybrid fiber mode **EH$_{11}$** is a crucial aspect to achieve a proper spectral broadening. When a linearly polarized Gaussian beam is injected into a hollow fiber on axis, only the **EH$_{1m}$** modes in the fiber are mostly excited [28]. The coupling efficiency η_{11} into the fundamental fiber mode is given by

$$\eta_{11} = \frac{\left| \int_0^D exp\left(-\frac{r^2}{w_0^2} \right) J_0 \left(2.405\frac{r}{D} \right) r \cdot dr \right|^2}{\int_0^\infty exp\left(-\frac{2r^2}{w_0^2} \right) r \cdot dr \int_0^D J_0^2 \left(2.405\frac{r}{D} \right) r \cdot dr}, \quad (2.20)$$

where w_0 is the beam spot size at the beam waist and D is the core radius of the fiber. In order to maximize the coupling efficiency, the ratio w_0/D has to be around 0.64 [25]. In the experimental setup for this project, the hollow fiber is 1 m long with a core diameter

of $250\ \mu m$. The gas used was Neon at approximately 1900 mbar. Looking at the equation 2.20, the reader can then understand how fluctuations, spatial displacements, can greatly affect the dynamics of the coupling process and then the pulse spectral broadening. In this point resides the aim of the stabilization project performed.

Self-Phase Modulation

SPM is a nonlinear optical effect and in this project it is performed in the hollow fiber. A detailed mathematical descriptions of the pulse propagation and the related equations will not be presented here, but rather a conceptual description of the phenomena belonging to the group of third-order optical effects. Self-phase modulation is the change in the phase of an optical pulse resulting from the intensity dependent refractive index of the material within which the beam propagates [29]. In fact, the time dependent refractive index assumes the following expression:

$$n(t) = n_0 + n_2 \cdot I(t), \tag{2.21}$$

where n_2 is the nonlinear refractive index and $I(t)$ is given by equation 2.7, where:

$$\begin{aligned}
I(t) &= \epsilon_0 c n \frac{1}{T} \int_{t-T/2}^{t+T/2} |\tilde{E}_p|^2 (t') dt' \\
&= \frac{1}{2} \epsilon_0 c n \mathcal{E}^2(t) \\
&= \frac{1}{2} \epsilon_0 c n \tilde{\mathcal{E}}(t) \tilde{\mathcal{E}}^*(t),
\end{aligned} \tag{2.22}$$

giving

$$n(t) = n_0 + \frac{1}{2} n_2 \epsilon_0 c n |\mathcal{E}(t)|^2, \tag{2.23}$$

that is only dependent on the envelope profile, proportional to the squared of the electric-field envelope. The phase shift causing the spectral broadening can be expressed as a change of the instantaneous frequency, introduced before in equation 2.12. Considering its differentiation with respect to time, one obtains

$$\frac{d\Gamma(t)}{dt} = \omega_l + \frac{d\varphi(t)}{dt} \tag{2.24}$$

where it can be underlined the second term, that is causing the nonlinear phase shift:

$$\delta\varphi(t)_{\text{NL}} = \frac{d}{dt} \varphi(t)_{\text{NL}}. \tag{2.25}$$

If one thinks about the pulse phase term $\Gamma(t)$, the nonlinear terms in its derivative is the only time-dependent phase term $\varphi(t)$: this explains why the index remarks the

nonlinearity [29]. The SPM plays its role as the principal nonlinear effect over the hollow fiber length:

$$\varphi_{NL}(z,t) = -\frac{k_l n_2}{n_0} z I(t) = -\frac{\omega_l n_2}{c_0} z I(t), \tag{2.26}$$

where z is the coordinate along the direction of propagation and $k_l = \omega_l/c = (\omega_l n_0)/c_0$ is the angular wave–number. Combining equations 2.25 and 2.26, the instantaneous frequency shift is given by:

$$\delta\varphi(z,t)_{NL} = -\frac{\omega_l n_2}{c_0} z \frac{d}{dt} I(t). \tag{2.27}$$

where the space dependence of the phase variation has been introduced, which will equal the length of the fiber in this context.

The spectral changes introduced by SPM are a direct consequence of the time dependence of the nonlinear phase term of the pulse. This modulation is a *frequency chirping*. The chirp introduced by this effect increases in magnitude proportionally with the distance of propagation, as shown in equation 2.26. New frequency components are generated continuously along the propagation in the hollow fiber, broadening the pulse spectra profile [26]. If it is considered the case in absence of dispersion and self–focusing, the maximum broadening achieved over a length L of the pulse bandwidth will be

$$\Delta\omega_{p,max} = 0.86\gamma P_0 \frac{z_{eff}}{T_0}, \tag{2.28}$$

where $z_{eff} = [1 - \exp\{-\alpha \cdot L\}]/\alpha$, P_0 is the pulse peak power and T_0 is the half–width at the $1/e$ intensity point. The attenuation coefficient α is given in equation 2.19 [24,26].

2.5.2 Pulse Temporal Compression

Phase dispersion compensation: The Chirped Mirrors

Once the spectrum is broadened enough to sustain few–cycles optical pulses, dispersion compensation of the frequency chirping introduced by SPM has to be performed. In order to compensate this phenomenon, several optical setups can be employed: in the Attolab three pairs of chirped mirrors are disposed at the output of the fiber. Mirrors used to reflect laser light are in general dielectric mirrors composed of alternating high and low index quarter wavelength thick planes, that produce a strong Bragg-reflection. Chirped mirrors are structured in order to achieve a chirped Bragg wavelength depending on the depth: different wavelengths penetrate different depths into the mirror, being reflected by the layer at that particular depth. After each reflection there is a compensation of the initial dispersion since a group delay is introduced. There are two main reasons to employ

chirped mirrors. The first resides in the broad high-reflectivity bandwidth of the mirrors. The second is the dispersive properties of these mirrors; their ability to compensate the chirping by introducing a compensating group delay.

2.6   Carrier-to-Envelope Phase Offset and CEP locking

As discussed in subsection 2.3.1, the carrier-to-envelope phase ϕ_{CE} of a pulse is defined as the difference between the phase of the carrier wave and the envelope peak position, the latter being converted to a phase value. During the pulse propagation through a
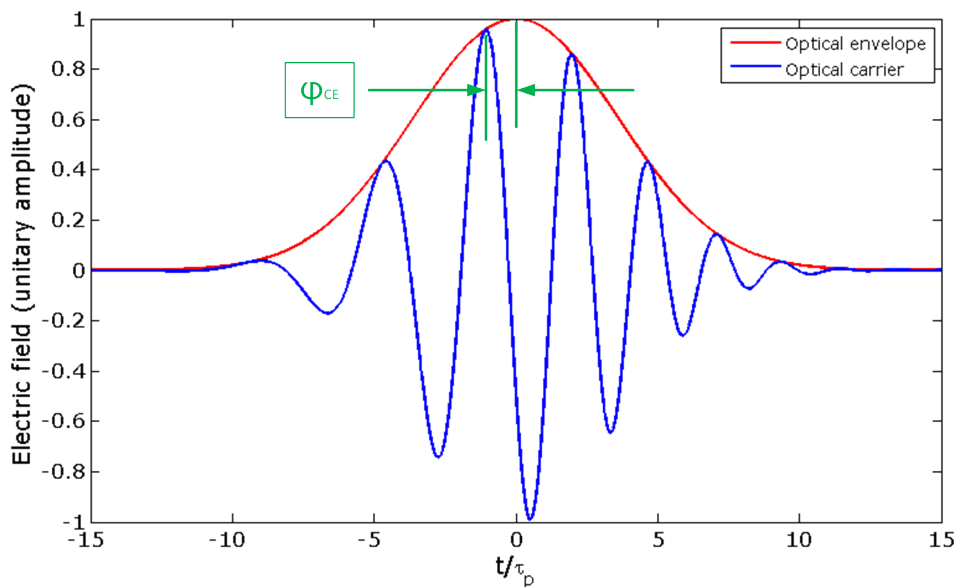

Figure 2.6: The Carrier to Envelope Phase is the phase shift between the peak of the optical envelope and the carrier. Explicative plot realized in Matlab.

medium, the relative position between the carrier wave and the envelope will in general change due to chromatic dispersion, causing a difference between the phase velocity and the group velocity, and sometimes also due to optical nonlinearities, *e.g.*, the SPM in the hollow fiber [17, 30]. It follows that ϕ_{CE} evolves during propagation due to this "slipping" between the carrier and the envelope.

The seed oscillator, model Femtolasers *Rainbow*, is CEP-locked: a stabilization technology that provides at the output the same phase every 4th pulse. But after the oscillator, the pulses characteristics change over the optical path, and after all the amplification and shaping, and also due to mechanical vibrations and intensity variations, additional jitter and drift of the CEP is introduced.

In a mode-locked laser, a pulse train is usually generated from a single pulse cir-

culating in the laser resonator. Every time when this pulse hits the output coupler, an attenuated copy of it is emitted. Typically, there is a certain change in the CEP-offset in each round trip, which can be hundreds or thousands of radians. Therefore, each emitted pulse will have a different carrier-to-envelope phase [17, 30], that is impossible to measure in absolute terms. Since after the oscillator the laser is further manipulated, at the compressor exit it is necessary to re-stabilize the CEP-offset. This needing has been fulfilled applying an external feedback loop control, actuated by an acousto–optic programmable dispersive filter [6]: considering two consecutive pulses and measuring the difference between the two phase values, the CEP-offset is obtained and used as set-point for the feedback loop.

It has mentioned that the stability of the phase is improved if a good stabilization of the pulse energy and pointing is introduced. This is the reason why the power-locking implies multiple advantages to the laser behavior, and that is an additional reason underlining the importance of the stabilization project performed in this work [7, 28].

Chapter 3

Control System and engineering

The Control System has been designed using a fast and powerful device as the main component of the entire project: the Field-Programmable Gate Array (FPGA). In this project, a "Noise Eater" has been developed. A user friendly FPGA board has been used, allowing to program three parallel Proportional-Integrative-Derivative (PID) controllers: two for the Beam Pointing Stabilization and the third for the Power Locking. The control system is composed of the National Instrument FPGA and other essential components: the detector for the laser pulses position with a signal processing circuit, a piezo-electric mirror for the beam pointing control and an acousto-optic modulator for the power locking with the respective drivers. In this chapter a description of the control system is presented and all the devices specifications follow.

3.1   The control problem

In order to design a stable and efficient control system, it is essential to represent and describe it as a linear system. In fact, the phenomena to be controlled in this application match the hypothesis; thus, it can be described mathematically with linear operators. Whenever there is a control problem, it is necessary to find out the different components that play a role in the phenomena.

In figure 3.1 the following problem can be seen: given the system P and measurement signals y, determine the control signals u such that the control objective z follows the reference r as "close as possible" despite disturbances w, measurement errors n (noise etc.) and uncertainties of the real process.

Behind this important passage about the block diagram resides the concept of *feedback control*. In fact, if one tries to imagine a situation that fits the control problem mentioned above and associate the action of each component in a chronological order, it is clear
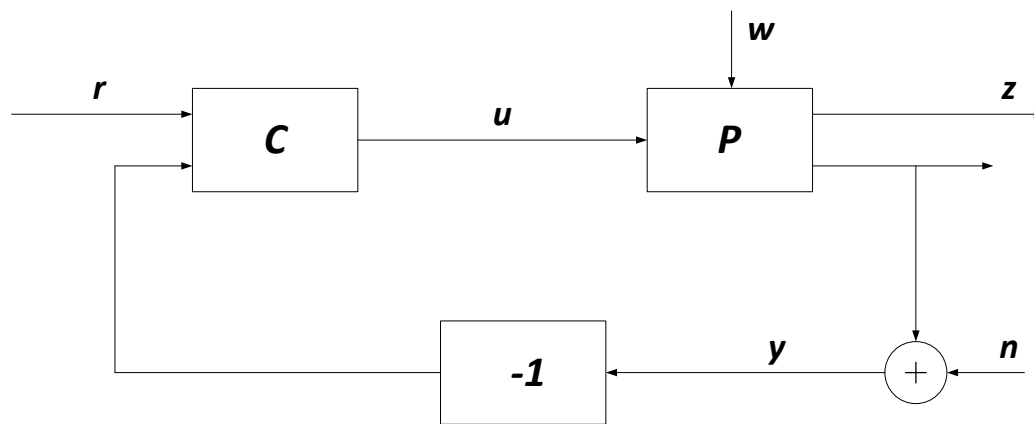
Figure 3.1: Generic block diagram representation of the control problem.

that the control signal *u* is *calculated* after the measurement of the process. Only once a measurement has been made, a **controller** can produce an action to reduce, as much as possible, the **error**, which equals the difference between the process signal and the reference. For this specific reason the term **feedback** control is used. Specifically, this case presented is called **closed-loop feedback** control since in the diagram the ring representing the loop is closed. Feedback control provides an action able to maintain certain process conditions by measuring the difference between the actual conditions and the desired ones. This kind of broadly used technique is basically a human routine, reproduced in automation technology: for example, if one thinks about how we move or how we keep the equilibrium of our bodies, the schematic of the feedback control matches as a descriptor.

Applying the control problem to the case of ***pointing stabilization*** (figure 3.2a on the next page), it is appropriate to translate the problem as follow: given the system *P* – representing the laser beam position – and the measurement signals *y* – representing the measured position of the laser beam – determine the control signals *u* such that the control objective *z* – representing the real position of the laser beam – follows the reference *r* – the set-point of the laser beam position – as "close as possible" despite misalignments of the optical setup *w* and electronic noise affecting the measurements *n*.

The same can be done for ***power stabilization*** (figure 3.2b on the facing page): given the system *P* – representing the power fluctuations – and the measurement signals *y* – representing the measured relative power level – determine the control signal *u* such that the control objective *z* – representing the real power level of the laser beam – follows the reference *r* – the setpoint of the power value desired – as "close as possible" despite

instabilities (sources of power laser noise) of the optical setup *w* and electronic noise affecting the measurements *n*.
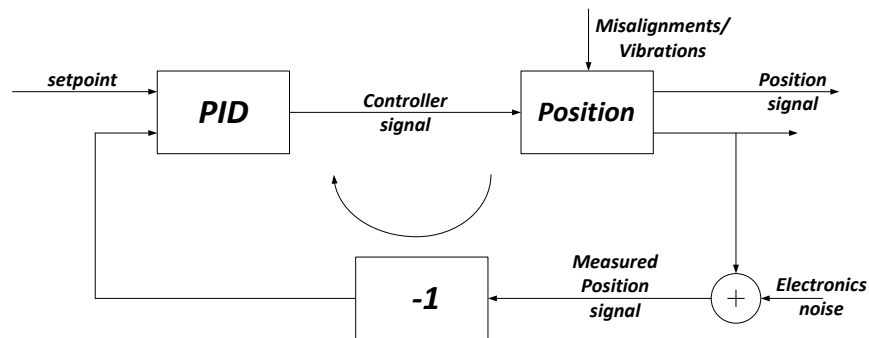
(a) *Block diagram related to the beam pointing control problem.*
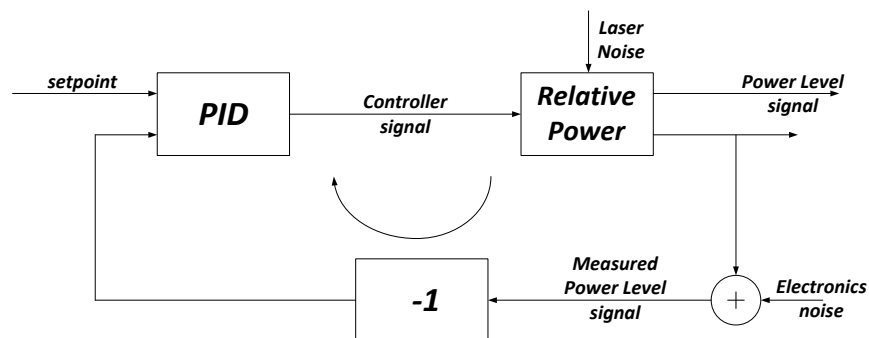
(b) *Block diagram related to the power control problem.*

Figure 3.2: The feedback controller developed for the project intended to stabilize both sources of instabilities: beam pointing and power fluctuations.

Within the stabilization setup developed, several components and devices are used in order to achieve the proper actuation of the feedback control. In fact, as introduced by the block diagrams, all the processes signals in this context are analog signals coming from detectors and handled in order to output another analog signal, the control signal. The components having a central role can be divided into four groups:

- Detection;

- Sampling and signal processing;

- Calculation of the Control Signal;

- Actuation.

In the next sections a brief description of the devices performing the above listed actions is given. Some of the specific information is taken from their respective manuals.

3.2   Detection: The Position Sensitive Device

For the detection of the laser beam position and the power level, a common kind of optical detector is used: the position sensitive device (PSD). Such optical sensors are nowadays widely used in a multiple of photonics applications. The PSD used in this work is made by Hamamatsu Photonics K.K., Solid State Division from Japan, and it belongs to the category of isotropic raster–like surface sensors. This category has a surface able to provide continuous position data; the other category has a surface made by sub-sensors supporting local discrete position data. The model used for the configuration is a two–dimensional PSD (model S2044) having an active size of detection equal to 4.7 mm $\cdot 4.7$ mm. The relative power level is acquired as well since the detector, by its engineering, gives a sum signal representing the photon flux hitting the active area of the detector. Optical position sensitive detectors can be seen as photodiodes able to measure the centroid position of a light spot striking their surface. The position information is calculated through a balance of the different photocurrent values in the x– and y–directions.
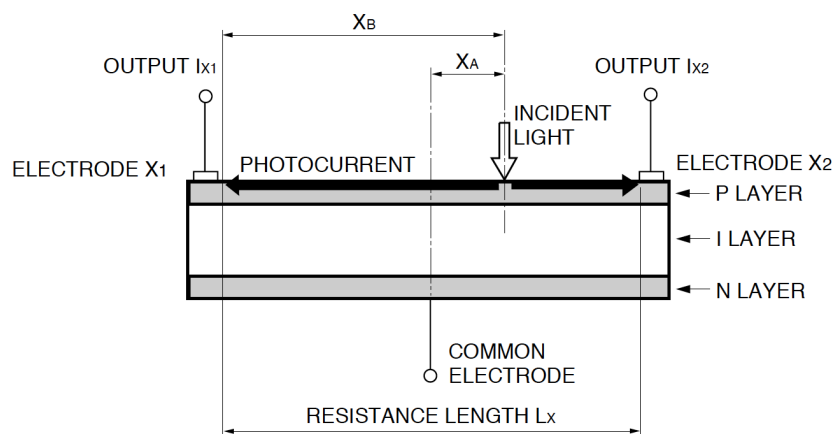

Figure 3.3: Cross section of a position sensitive device. Image from Hamamatsu Photonics, KPSDC0005EA

Basically a PSD has a slightly different structure than a photodiode. As illustrated in figure 3.3[*], the structure represented suggest the general scheme of a PIN–diode, a common electronics component.

It is composed of a p–type[†] uniform resistive layer formed on an high–resistive intrinsic silicon substrate. On the two lateral edges two output electrodes are formed. On the other side of the package, an n–layer is attached and connected on the backside to a common

---

[*]Image from S1880,S2044 PSD Datasheet.
[†]In Microelectronics doped semiconductors adding carriers (electrons, hence, donors) are briefly called n–type. Acceptors doped semiconductors are named p–type.
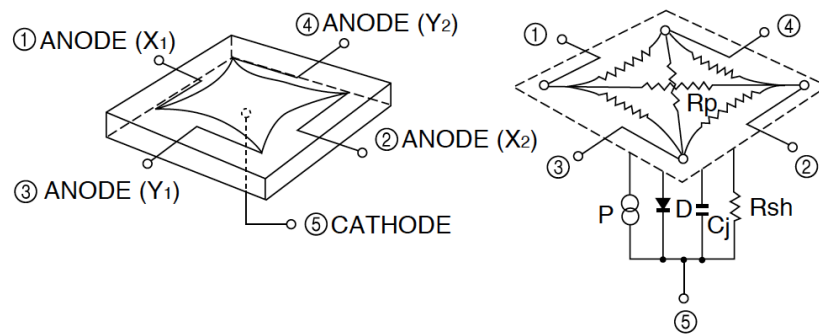
Figure 3.4: Representation of a two-dimension pin-cushion tetra-lateral PSD. Image from Hamamatsu Photonics, KPSDC0009EA

electrode. When a pulse of light strikes the active surface (the p-type resistive layer), an electric charge is generated at the incident position that is proportional to the energy of the light pulse. This electric charge is carried by the resistive layer and collected by the two output electrodes X_1 and X_2 as photocurrents (expressed later as I_{X_1} and I_{X_2} respectively). The photocurrent is dived in inverse proportion to the distance between each electrode and the incident position of detection. This yields a certain value of
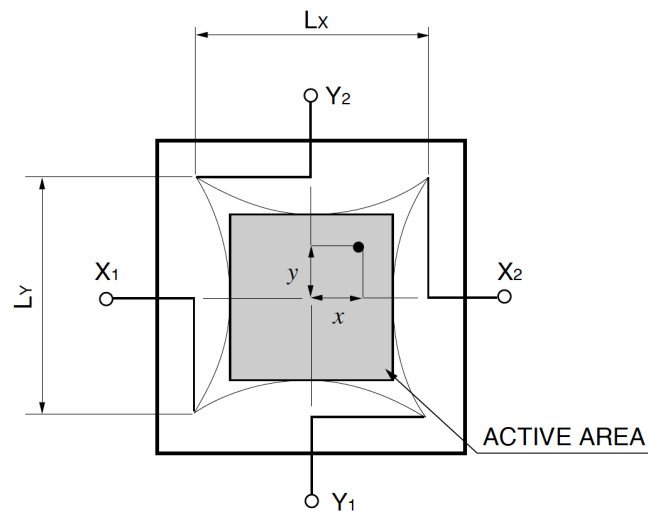

Figure 3.5: Representation of the active area of the tetra-lateral type PSD used in the detection setup. Image from Hamamatsu Photonics, KPSDC0009EA

current at each output, and when processing this signal it is possible to compute the incident position once one has fixed a reference. Finding the difference and then the ratio between the two output photocurrents, the position of the incident light can be calculated using specific formulas for the specific architecture of the PSD. An important aspect is that the measure obtained is independent of the quantity of photons striking the detector,

in other words, the measure is not affected by a change of the incident light intensity. The model S2044, which is sketched in figure 3.4, is a tetra-lateral type PSD with an improved active area and a reduced interaction between the different electrodes. Being a 2D PSD, it is composed of four electrodes at the edges; hence four different photocurrents. The conversion formulas to obtain the geometrical position, represented in figure 3.5, are expressed in eqs. 3.1 and 3.2:

$$x = \frac{L_x}{2} \cdot \frac{(I_{X_2} + I_{Y_1}) - (I_{X_1} + I_{Y_2})}{I_{X_1} + I_{X_2} + I_{Y_1} + I_{Y_2}} \qquad (3.1)$$

$$y = \frac{L_y}{2} \cdot \frac{(I_{X_2} + I_{Y_2}) - (I_{X_1} + I_{Y_1})}{I_{X_1} + I_{X_2} + I_{Y_1} + I_{Y_2}}, \qquad (3.2)$$

where the variable expressed can be identified by looking at figure 3.5 on the preceding page. An important aspect when a sensor is exploited consists of verifying and calibrating its physical limitations. Knowing these characteristics, it is possible to figure out the capabilities of the instrumentation. As discussed so far, the PSD surface gives to the electrodes different photocurrents and by making calculations upon these values gives an estimate position of the incident spot of light. The position obtained by this procedure gives the center-of-gravity of the light spot and it is independent of the beam spot size, shape of the laser spatial modes and intensity. As for all detectors, the measured light position can be slightly different than the actual position of the laser pointing. This source of inaccuracy is known as *position detection error*. When a laser beam strikes the *electrical center* of the PSD, the two extracted currents from the electrodes are equal. If one thinks to fix the electrical center as the origin of the system of reference, the detection error corresponds to the difference between the actual position of the laser pointing (X_i) and the calculated position from the PSD outputs (X_m, given by equation 3.1):

$$E = X_i - X_m [\mu m] \qquad (3.3)$$

In the case of the stabilization system developed, this source of error is irrelevant, since the position detected is a relative position to be kept over a long time. The purpose is to contain as much as possible the fluctuations around this relative position in order to increase the stability of the hollow fiber compressor: for this reason the absolute accuracy on the actual position of the beam position is not fundamental. Concerning the power stabilization, the photocurrents extracted from each electrode of the 2D PSD are summed in order to obtain the total photon-flux striking the detector, hence this kind of error does not affect the measured power level. The four photocurrents extracted from the

PSD are processed and sampled by a signal processing circuit, which will be described in the next section.

Another essential aspect is the *position resolution*. For the PSD, the position resolution is the minimum detectable displacement of the center-of-gravity of the laser position, expressed as a distance on the detector surface. For the model used a resolution of 0.6 μm is specified for a spot of light having a diameter of circa 200 μm, which is roughly the same as for the setup used in the present thesis project. This value is proportional to the length of the PSD (in the two directions) and to the noise of the measuring system, while it is inversely proportional to the photocurrent ($\propto$ light intensity) of the PSD [31].
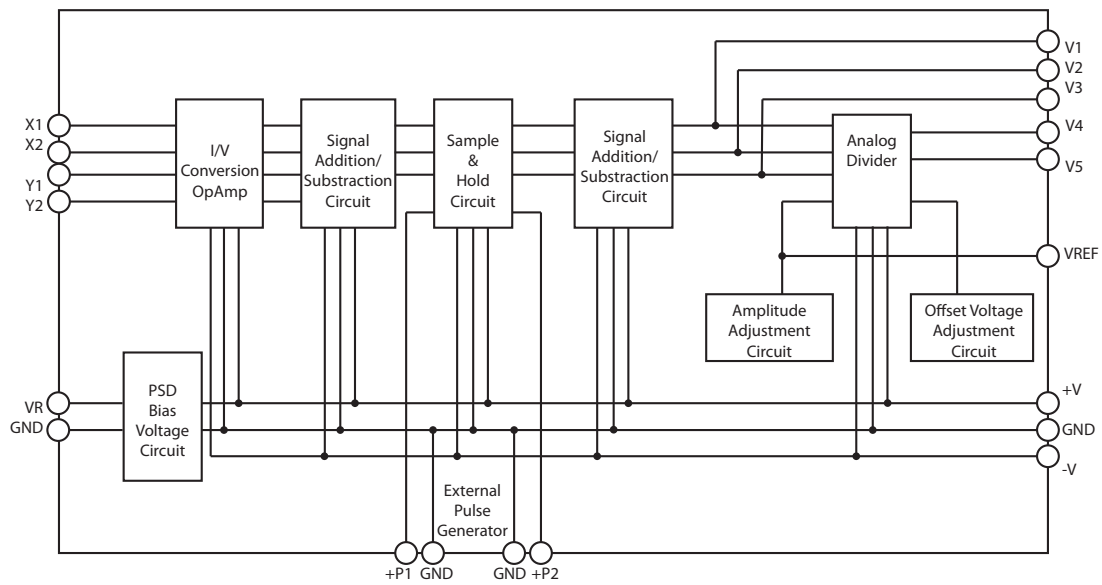

Figure 3.6: Block diagram of the signal processing circuit Board for AC pulse signal detection.

3.3   Sampling and signal processing

In order to facilitate the operations of the position sensitive device a signal processing circuit has been provided. The producer is the same as for the PSD (Model N.C7563), and the circuit comes with all the mounting instructions to arrange the specific PSD on the board. In figure 3.6 a schematic block diagram of all the sub-circuits of the board is represented, and what follows is a brief description for each of those roles. Looking at figure 3.6, at the first step the outputs of the PSD are converted from electric currents to voltage signals. This process is provided to increase the noise rejection and to treat each signal easier in the successive steps. After the signals are converted, the operational part

takes place and the different voltages are combined by the summing-dividing block circuit implemented on-board. The result of this step is the extraction of three different signals
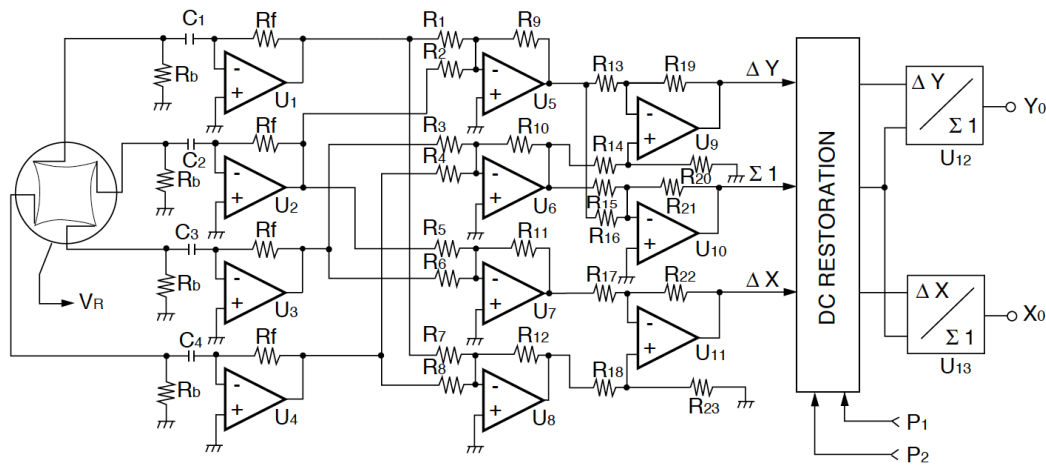

Figure 3.7: Sub-circuit of the Signal Processing Board that schematically show the first operational part of the Board. Image from Hamamatsu Photonics.

representing the two ***differential position values*** and the ***relative intensity level*** striking the resistive surface of the PSD: ΔX, ΔY and Σ_1. It has to be remarked, that the relative power level is exactly the current-voltage conversion of the sum of the electrodes currents extracted from the PSD. This is an important aspect because the algebraic electronics operations in the processing circuit, which result is expressed on the output in figure ??, correlate the displacements signals with the relative power level signal. Basically power fluctuations introduced an additional error in the position detection.

Since the signals are pulsed, the board includes a synchronous block circuit that implements the ***Sample & Hold***. The board is designed with an internal clock that should be used to trigger an external light source with a repetition rate of 333 Hz. This configuration does not fit with the laser source intended to be measured here; the laser must trigger the detection an not the other way around. For this reason some modifications to the board have been done. All the schematics and the instructions to modify the board and to make it suitable for the femtosecond laser were suggested by Akira Suda at the RIKEN Center of Research, Yokohama, Japan. The modification consits of opening two circuit lines connected to the S&H integrated circuits (ICs), and to replace these with two external ones generated by a SRS delay box (Model DG350), and carried by two BNC cables.

The process of S&H is really intuitive and easy to understand. Figure 3.8 shows how

it works. The first TTL pulse P_1 from the delay box activates the first S&H IC, named
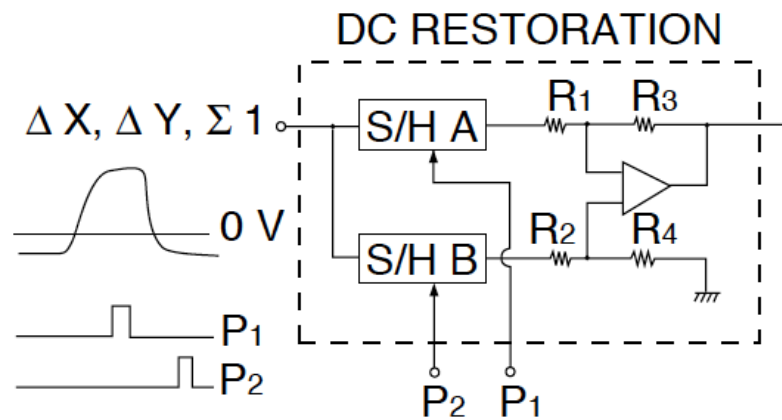

Figure 3.8: Scheme showing the process of S&H and how the pulse light is differentiated from the "dark" threshold, (the 0V level). Image from Hamamatsu Photonics.

in the figure *S/H A*, which samples the signal at its peak value. The signal sampled and held by the second IC *S/H B*, which is activated by the second external pulse P_2, is subtracted from the value held by *S/H A*. Therefore, the board calculates the differences for each pulse of light between the *"light"* value with the corresponded value at the *"dark"* level. The task of the following ***analog divider*** block is to give at the outputs the voltage values directly proportional to the position values for each orientation. This relation is represented in figure 3.9: two settings are available, of which the more sensitive one has been chosen [32].

3.4   Calculation of the Control Signal

3.4.1   PID: The Proportional–Integral–Derivative controller

The controller for the two processes is a Proportional-Integral-Derivative Controller. It is the most used algorithm in industry and technology for any kind of automatic control. The popularity of PID controllers can be attributed partly to their robust performance in a wide range of operating conditions and partly to the simplicity of their adaptation to the process to be controlled. It is exactly for this reason that engineers use PID controllers in a straightforward and broad manner. In general, it can be asserted that most of the *control objects*, also called *"plants"*, can be approximated with first– or second–order systems; they can be modeled adequately by respective order differential equations. The PID is a perfect
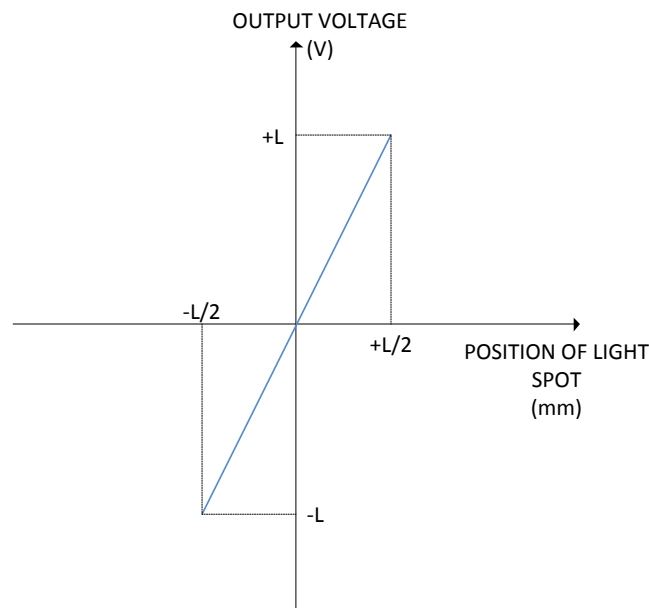
Figure 3.9: Relation between the output voltage of the signal processing circuit board and the real position on the sensor surface of the light spot. The conversion factor is $1/2$; L is a generic magnitude number.

tool, once it is tuned properly, to control such systems. Now think about a simple case where the process to control is a static system with a gain K_p. For a proportional–only controller, the output u is the product of the error signal and the *proportional gain* K_c:

$$u(t) = K_c \cdot e(t) = K_c \cdot (r - y(t)). \tag{3.4}$$

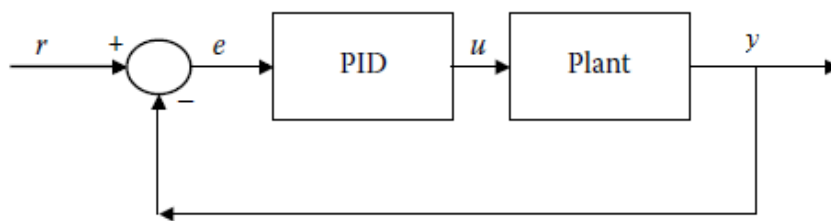The different variables are defined in section 3.1 on page 31. The closed–loop response

Figure 3.10: Scheme of the simple proportional–only controller.

can be drawn as the relation between the system variable y and the reference signal, or set–point, r, representable as:

$$y = \frac{K_c K_p}{1 + K_c K_p} \cdot r \tag{3.5}$$

Ideally when $K_c \to \infty$, which means that the gain is increased, then $y \to r$. In addition to the proportional mode, the derivative action will now be added. The controller output

is:

$$u(t) = K_c e(t) + T_d \frac{de(t)}{dt} \qquad (3.6)$$

where T_d corresponds to the *derivative gain*, and it is the time of differentiation of the time–dependent error signal. An important aspect to underline is the sensitivity to noise of this controller component. In fact, differentiating high–frequency noise gives as a result an amplification of it. The global effect is that the controller output can become cyclic or unstable giving a detrimental effect on the longevity of the actuators. In fact, it is introduced only for fine tuning of the controller in the present application. The action of the proportional–derivative controller is represented in figure 3.11, where the step response of such a system is shown, together with the error signal and its derivative. The top graph shows the process variable, desired to be at the reference level of 1. The step response is how the control system, the PID, reacts to a step–function input. In the second graph the error is represented, showing the difference between the process variable and the reference value. Finally, in the last graph, the derivative of the error is plotted, which indicates the response speed of the control system.
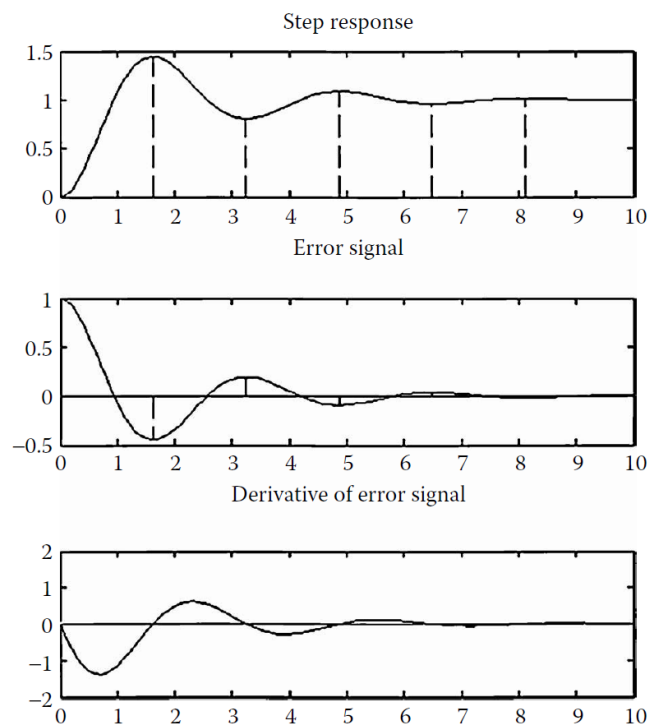

Figure 3.11: Representative graphs of the step response, the error signal and its derivative. Image from [33], page 109.

The final and probably the most important component of the PID controller is the integral mode. Almost all kind of controllers implement some sort of integral action. It is

really important because its contribution is to give as output the accumulated error, which is the area under the error signal curve. If the error variable goes to zero, the output of this controller component will be constant and equal to the cumulative area calculated up to that point. When this condition happens the outputs from the proportional and the derivative terms will be equal to zero and the only value outputted will be the one of the integral term. Summarizing the three terms explained, the time–domain equation giving the controller output of the PID controller is:

$$u(t) = K_c \left(e(t) + \frac{1}{T_i} \int e(\tau) d\tau + T_d \frac{de(t)}{dt} \right). \tag{3.7}$$

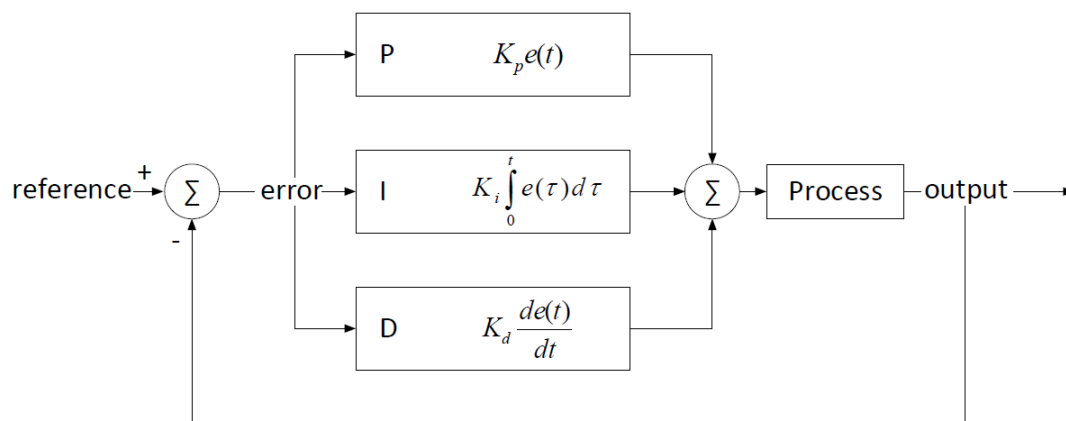A block scheme is represented in figure 3.12. An essential aspect to point out regarding

Figure 3.12: Block diagram of the PID controller with each of its terms. As it can be seen the three constants are named as K_p, $K_i = K_p/T_i$ and $K_d = K_p \cdot T_d$.

PID controllers, which is also a matter of interest for all kinds of controllers, is the *tuning*. Controllers are designed to avoid a continuous intervention of an operator over the process to be controlled, as explained before. The continuous action provided by a controller is guaranteed by its tuning. The better the choice of parameters K_p, K_i and K_d, the better the maintenance of the stabilization. The obstacles to achieving the goals come generally from the disturbances; in this project these factors are the load disturbances (attributable to intensity noise for the power and mechanical and thermal drifts) and the feedback noise of the entire controller system. In many cases also the set–point can be a source of problems, but in the present case, the value is kept constant, excluding the reference from the group of disturbance contributors.

3.4.2 FPGA and LabVIEW™: how and why

As introduced above, in order to develop and provide a suitable and flexible PID controller for the project purposes, the best solution was to use a field programmable gate array from National Instruments™. The wonderful characteristic of this kind of integrated circuit device is the easy programmability, reliability and the speed with which the operations are computed. Instead of really complex low-level programming languages[‡], a module extension for LabVIEW™ that enables an easy graphical Virtual Instrument file programming is used. The friendly approach that the user can obtain using graphical programming is not comparable to any other programming syntax approach, and for this reason NI products are widely used in laboratories and industries. Once the VI[§] is created, the NI FPGA Module compiler translates it into a lower level language and then to a bitstream flux written to the FPGAs logic matrix gate circuitry.

In order to define the action of a general FPGA IC, the user has to provide the *hardware description language* (HDL) or a schematic design; one example of this schematic is exactly a NI Virtual Instrument. There are pros and cons about these two ways to approach the programming of this amazing piece of technology, *e.g.*, for the HDL programming it can be stated that it is more suitable for large algorithms because each programming part is specified by number instead of graphical instructions. However, graphical structuring provides an easier visualization of the designed ensemble of instructions. The FPGA model used for the implementation of the PID algorithm is the NI 7833R that provides eight independent 16-bit analog-input (AI) channels, and the same kind and amount of analog-output (AO) channels. The board is mounted on a regular personal computer through PCI bus and the FPGA IC included is a Virtex-II XC2V3000 with three millions logic gates. In order to link the input signals coming from the signal processing circuit to the FPGA board, a configurable connector box (Model SCB-68) produced by National Instrument is used. This connector box gives the possibility to decide for each input the type and the level of filtering: low-pass or high-pass filtering. For the actual configuration, the system signals were not filtered physically: instead a Butterworth filter was implemented into the VI program of the FPGA, as it is shown in figure 3.13. The connection mode of the signals can be selected via software, from the configuration panel of the NI 7833R. In

---

[‡]The main producers of FPGA ICs build their own property syntax language. General further details on http://en.wikipedia.org/wiki/Field-programmable_gate_array.

[§]It is generally meant as Virtual Instrument, corresponding to the file extension of LabVIEW™ programs or subprograms.

fact, it is possible to connect the cables to the shielded connector box in differential mode, referenced single ended and non–referenced single ended. In this case it was decided to use the differential mode because this type of connection is suited for low voltage signals and has a better rejection and reduction of noise components affecting the action of the controller programmed in the FPGA VI. The PID algorithm implemented into the software is provided by National Instruments, and it provides a suitable and detailed configuration of the parameters and the general settings of the virtual controllers. In figure 3.14a on the facing page the portion of the code related to the beam pointing stabilization is represented. In figure 3.14b on the next page the power level algorithm is shown. The virtual PID implements a discrete algorithm, given by the formula:

$$u(n+1) \;=\; K_c \cdot \left\{ e(n) + \frac{T_s}{T_i} \cdot \sum_{i=0}^{n} e(n) - \frac{T_d}{T_s} \cdot \Delta y \right\}, \tag{3.8}$$

$$\Delta y \;=\; y(n) - y(n-1), \tag{3.9}$$
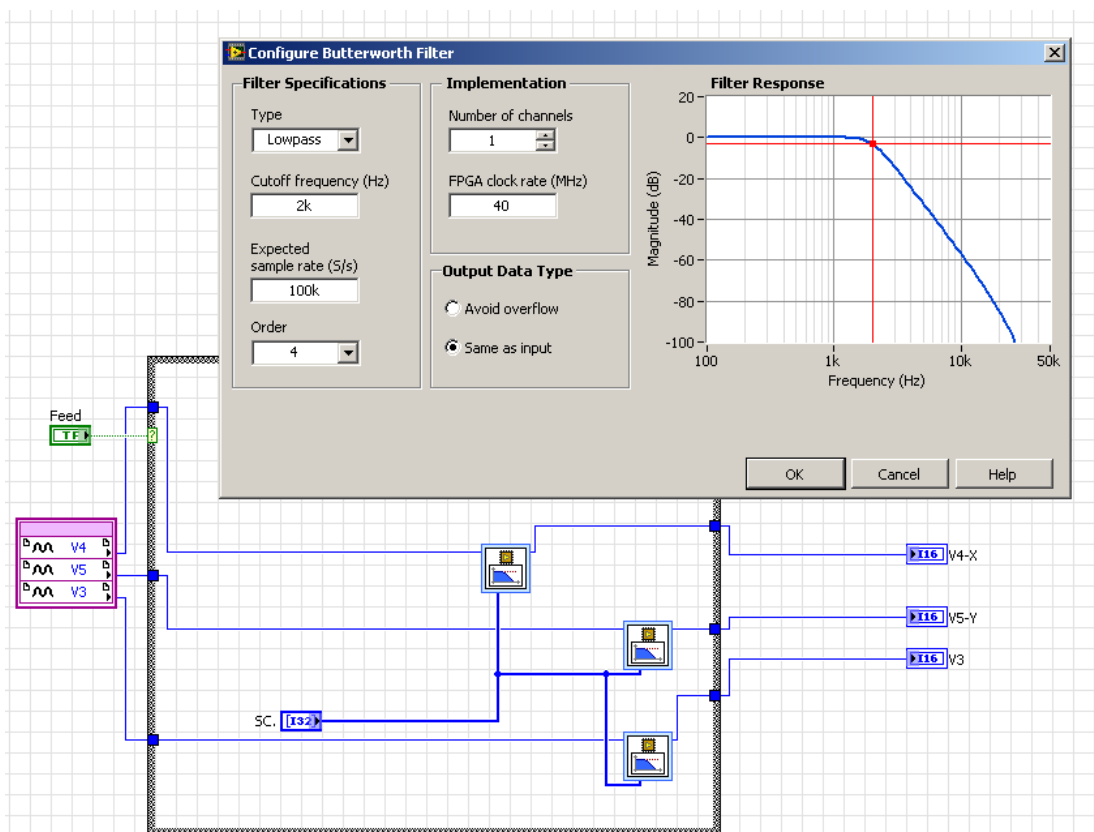
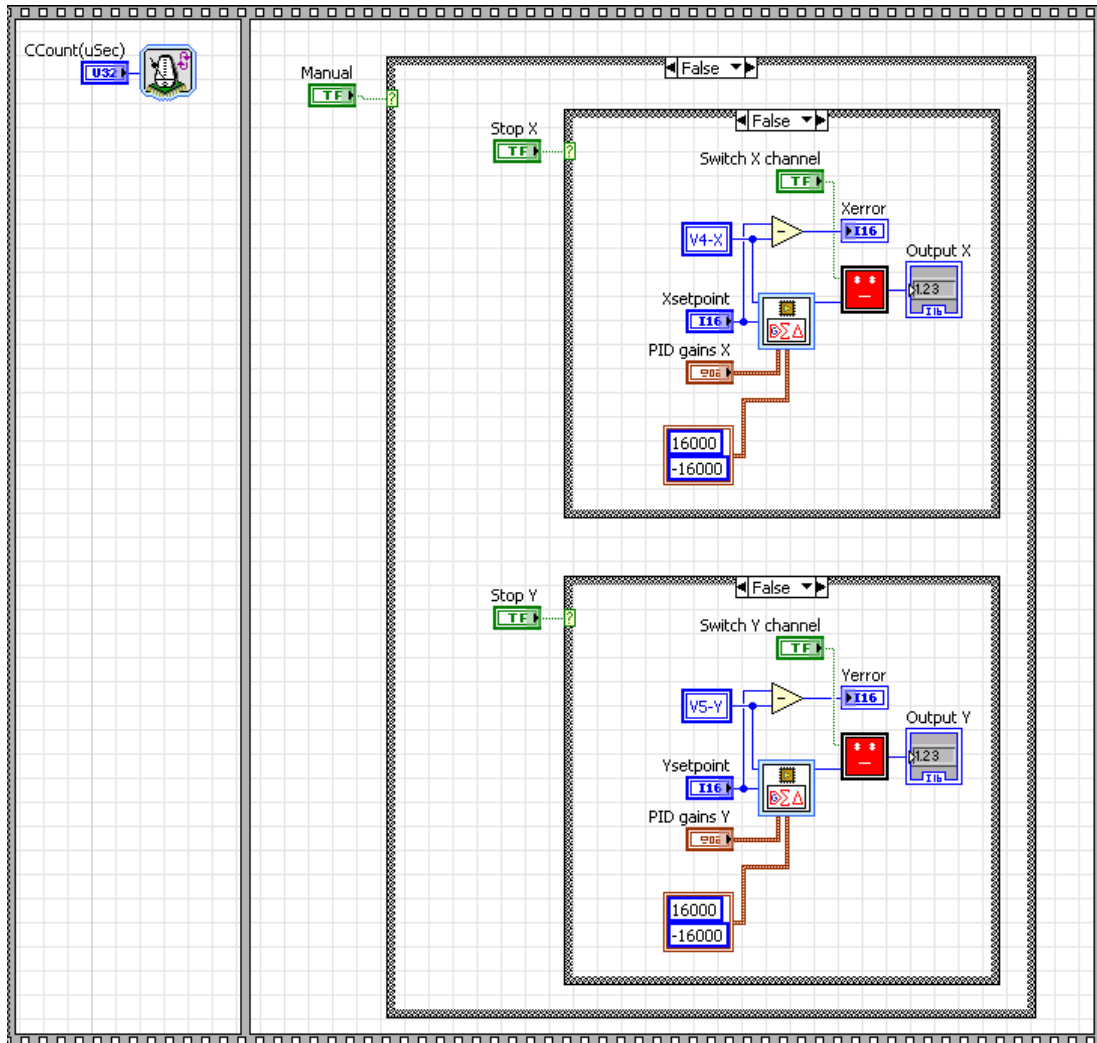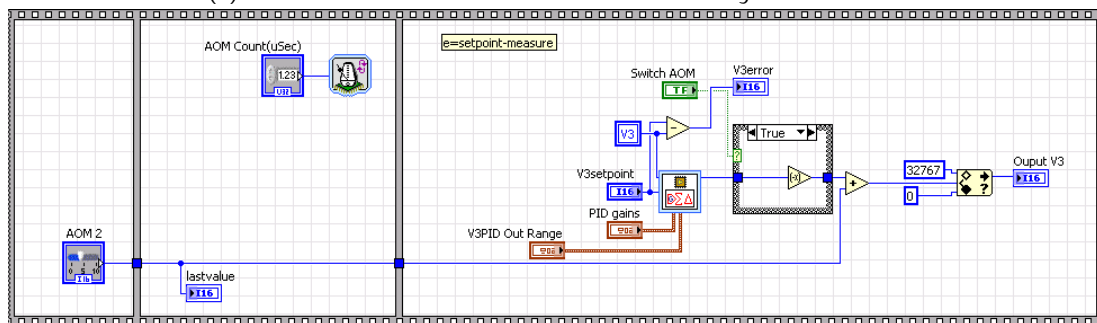$$e(n) \;=\; r - y(n), \tag{3.10}$$

Figure 3.13: Portion of the FPGA Virtual Instrument program. The sampled signals V4,V5 and V3, corresponding to the horizontal, vertical and relative power level, respectively, and they are filtered with the shown configuration of the virtual instrument Butterworth filter.

(a) *Portion related to the PID for the Beam Pointing Stabilization.*

(b) *Portion related to the PID for the Power Locking.*

Figure 3.14: The feedback controller developed for the project is software–based, designed, imple–
mented and compiled into the logic gates of the National Instruments FPGA.

where the parameters that are finally set on the computer program are:

$$P = K_c, \tag{3.11}$$

$$I = K_c \cdot \frac{T_s}{T_i}, \tag{3.12}$$

$$D = K_c \cdot \frac{T_d}{T_s}. \tag{3.13}$$

3.5   The Actuators

As mentioned in section 3.1 on page 31 the system is finally completed by the actuation of the control signals from the FPGA. For the beam pointing stabilization a piezoelectric mirror made by Thorlabs (Model KC1-PZ) has been used, driven by a high–voltage generator (Model MDT693A). On the other hand, for the power locking, a calibrated and aligned acousto–optic modulator made by IntraAction Corp. (Model ASM–805BL59) has been employed and driven by a light modulator signal processor (Model ME–803). A brief description of this two essential components follows.

3.5.1   The Piezoelectric Mirror

The piezoelectric mirror is a kinematic mirror mount and in the project has been mounted as one mirror after the compressor setup in the CPA system. This setup decision has been made in order to have the best performance in the optical setup. Practically, the high–voltage generator receives the control signals from the FPGA connector box and at the outputs gives high–voltage signals. The driver sends through two BNC cables amplified actuator signals to the electrodes of the piezoelectric mirror mount for the x– and y–axis. The mount is designed to be controlled over three axis, but in this application only the two main axis has been exploited: the horizontal (x) and vertical directions (y).

(a) *The piezoelectric mirror mount.*   (b) *The three-channels piezo driver.*

Figure 3.15: Laser beam pointing stabilization actuator. Images from Thorlabs.

   The driver inputs are comprised between 0 and 10 V, while the outputs are between 0 and 150 V. The algorithm inside the FPGA assigns the half scale input, and hence output, of the driver (5 V $\rightarrow$ 75 V) when the control signal is null, which means that no action is requested. This has been done in order to allow the controller to move the piezoelectric mirror back and forth on each axis to compensate for beam fluctuations in both directions.

   An important consideration in order to explain the limitations that this component

introduces to the system has to be done. The range of voltage oscillations of the driver imposes a condition on the frequency bandwidth of the piezoelectric mirror movements. Since the repetition rate of the laser is 1 kHz, to obtain shot–to–shot corrections, the frequencies of the kinematics of the piezoelectric mirror should fulfil this condition. According to the specifications given by the manufacturer and according to the dynamics of the driver signals, the frequency reachable for the piezoelectric is around 500 Hz, which is enough to achieve the desired conditions for stabilization but not sufficient for shot–to–shot corrections, so far achieved only by passive stabilization [34]. That value is further limited by the fact that the prevented bandwidth would be less in a closed–loop mode.

3.5.2 The Acousto-optic Modulator

The acousto-optic modulator (AOM) is a photonic device, usually referred to as a Bragg cell. This name is due to the fact that the central physical concept behind its functionality is the Bragg condition. The device is composed of a transparent material, within which an acoustic wave propagates in order to change the refractive index of the material. The interaction of light with the sound wave is explainable as an interference of the optical beam passing through the cell with the stratified parallel planes representing the refractive index variations originated by the acoustic wave. Here comes the Bragg condition: the set of parallel layers reflectors, separated by the sound wavelength Λ will reflect light if the angle of incidence of the optical beam θ satisfied the constructive interference ***Bragg condition***:

$$sin(\theta) = \frac{\lambda}{2 \cdot \Lambda},$$

(3.14)

where λ is the optical beam wavelength. This device can be used as a linear analog modulator since the intensity of the reflected portion of light is proportional to the intensity of
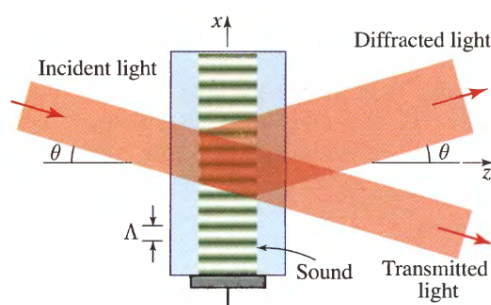

Figure 3.16: Representation of the Bragg cell. A sound wave applied to the cell acts as a beam–splitter when the angle of incidence θ satisfies the Bragg condition. Image from [35].

the sound wave propagating into the crystal. Hence, using an electrically driven acoustic transducer, the intensity of the reflected and transmitted light can be modulated [35].

In the control system setup the acousto–optic modulator has been mounted right after the multipass amplifier and before the grating compressor. The algorithm producing the control signal for the driver has been developed in order to set as a reference signal a certain value for the relative power level. Since the AOM can only remove light from the beam, the set–point has to be lower than the maximum value that the relative power level has at the moment of the tuning procedure for the system. Deflecting a fixed portion of the optical beam, the process signal can oscillate in both directions around this relative reference level since the power fluctuations can be compensated for an excess of optical power or even a lack of it.

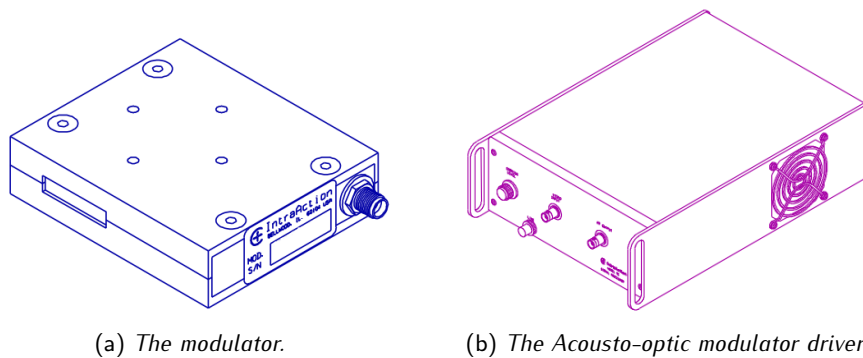(a) *The modulator.*   (b) *The Acousto-optic modulator driver.*

Figure 3.17: Power locking actuator schematic representation. Images from IntraAction Corp.

Practically the Bragg cell has been aligned in order to match the required optical condition. Further, to be able to interface the connector box of the FPGA with the acousto–optic modulator driver, a current amplifier has been built. This because the driver requires a higher current compared to what the FPGA connector box can provide. Hence, a nonlinearity can be introduced due to the not ideal behavior of the signal amplification besides the fact that the AOM response is much more nonlinear compared to the one of the piezoelectric mirror setup; for the performance obtained this fact has not been a limitation. The input of the driver is between 0 and 1 V, hence, providing the reference signal considering the fixed amount of deflected light, a voltage component is basically always present in the control signal. The frequency bandwidth of operation of the modulator is really high compared to the piezoelectric mirror action. In this case the limitation on the control of the power fluctuation frequencies is then the process variable signal. In fact the third output channel of the signal processing circuit board is the collected photon flux of

the detector, variable that is already affected by the beam pointing stabilization feedback being the denominator of the two position signals (see figure 3.7 on page 38), hence, the AOM frequency bandwidth is constrained by the other two channels.

Chapter 4

Experimental Setup and Results

The control system with all its components were installed and set in the Attolab once the control system started to respond positively. Below the layout of the control system in the laser setup will be described along with the achieved results.
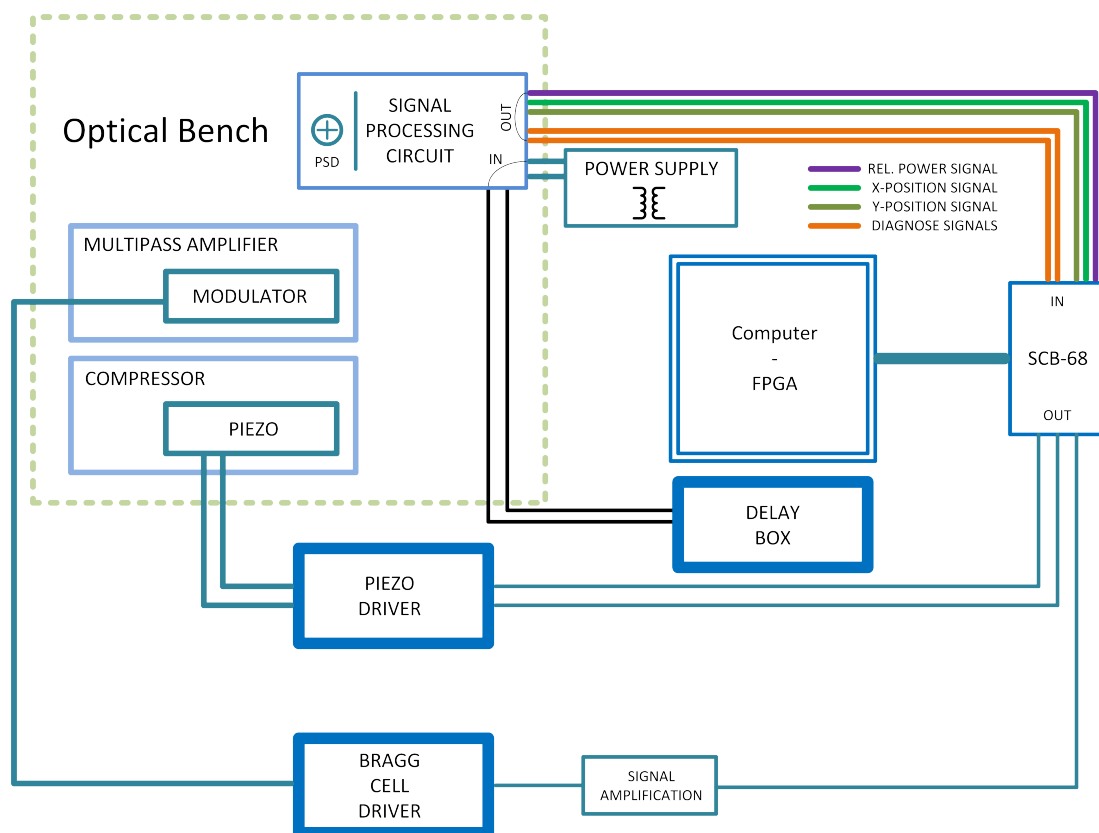
4.1 Experimental Setup

Figure 4.1: Schematic representation of the control system setup. The figure shows that the two actuators and the sensors are mounted on the optical bench, obviously along the laser path. The other components are disposed on the side of the optical bench.

In figure 4.1 an idea of the connections and the different main signals described in the previous chapter are presented. The computer includes the FPGA, which is connected to a PCI slot. A shielded cable links it to the connector box SCB-68. Inside the connector box the different input and output signal cables are connected to the board. The three main inputs (the two positions and the relative power) coming from the signal processing circuit are connected in differential mode, in order to have a good electromagnetic noise rejection. For the other two cables related to the indicators of the voltage reference and the voltage bias, a normal single-ended connection mode is used since they give just monitoring signals: for those wires the noise reduction is not a fundamental requirement.

The signal processing circuit has been shielded in an aluminium box. A small aperture has been drilled on the box cover at the exact spot where the position sensitive device is situated. The box is screwed on the bottom face to a couple of optical stirrups in order to let the aperture reach the laser beam height and to give to the entire structure a tight mount to the optical bench. The power supply cables for the ± 15 V DC are coupled in the main cable bundle of the signal processing circuit. Two BNC connectors have been made on one side of the aluminium box to connect the two trigger signals coming from the pulse generator (delay box, see section 3.3 on page 37).

The three outputs of the connector box are connected to the two actuator drivers through coaxial cables. The output control signal for the power is amplified before the driver since the output current of the FPGA board is too weak to drive the modulator, as mentioned in the previous chapter. Finally, the actuator cables are connected to the output ports of the drivers.

The two actuators and the signal processing circuit box are mounted on the optical bench, well aligned in their respective positions (figure 4.2). The piezoelectric mirror is installed as a reflective mirror after the laser system. Then the beam is focused by a lens (f=1.5 m) towards the hollow fiber. One leakage from one of the dielectric mirrors (in figure 4.2 is labeled M3) is used to obtain the measurements. In fact, this weak beam portion is then reflected and attenuated by neutral density filters (NDF) and used as a source of detection for the position sensitive device. An important optical considerations has to be taken in account: the PSD and the fiber entrance should be at equal optical distances from the piezoelectric mirror. The reason is clear: the fluctuations detected on the PSD surface have to represent as close as possible the fluctuations on the entrance quartz window of the fiber.

The choice to mount the piezoelectric mirror in that position is based on some basic geometrical optics reasons: since a 1.5 m lens is used to focus the beam for the fiber coupling, the angular misalignments corrections performed by the piezoelectric mirror are translated into proportionate planar drifts on the entrance of the hollow fiber, as much as on the PSD surface. For this reason accurate calibration of the detector position and piezoelectric mirror alignment have been crucial to reach a good response from the stabilization system. The host program, where the operator can set all the control parameters, takes measurements and it monitors the dynamics of the laser beam; it presents the possibility to manually control the piezoelectric driver outputs when the feedback action is off. This feature has been added in order to move and properly scale the range of possible movements on both axis, and to choose the optimal reference position for x- and y-direction, and to obtain a finer manual alignment for the hollow fiber coupling. Once the beam is well aligned in order to get a good detection on the PSD surface, the hollow fiber side of the optical path is aligned. Once the beam is well coupled to the fiber mode, the beam pointing stabilization system is turned on, keeping as reference signals for the two position control loops an average (on x and y) of 120 pulses detected around the position achieved during the manual alignment. The AOM is positioned along the beam
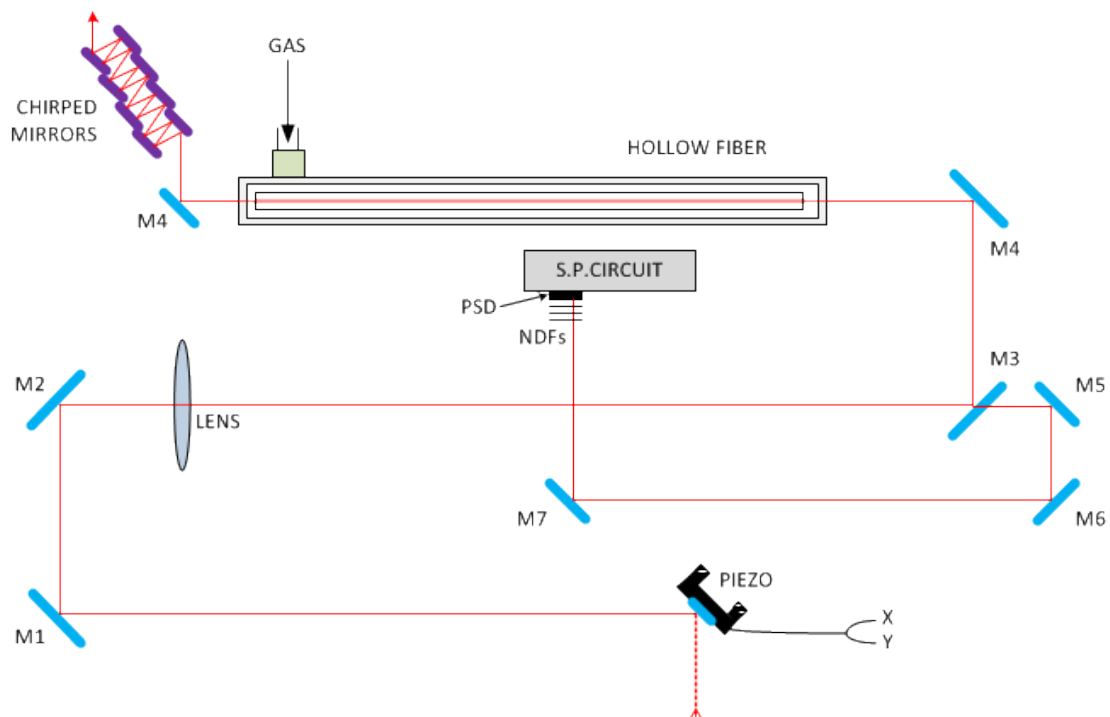

Figure 4.2: Schematic representation of the optical setup around the hollow fiber.

path in the cryo-cooled amplifier. Even for it the alignment requires precautions in order

to match the essential condition for the beam diffraction, as mentioned in the previous chapter. The driver can be manually controlled during the alignment process in order to see that the necessary Bragg condition is met. Also for the power controller it is possible to manually regulate the functionalities through the host front panel. What is basically done at the beginning is to observe the relative level of the pulses' energy on the host program; to increase the DC component of the acousto–optic driver in order to have a constant deflection of a portion of the laser beam, typically around 5%; set the reference signal value on the host and finally start the feedback loop. When the power stabilization is running, no iris should be used (or at least it should be completely opened letting the entire beam pass). In fact, if the beam is clipped by an iris, pointing fluctuations will be coupled to power fluctuations.

At the beginning of the work, the devices of the entire control setup were mounted on a separate bench. To test the device and the sensing, an He–Ne* laser was used. To be able to obtain $1\,\mathrm{kHz}$ pulsed source out of the continuous wave laser a chopper was employed, with a frequency regulation feature. Once the main electronics settings were done, the cable was manufactured taking care of the different noise reduction considerations, the system were calibrated and installed in the main setup in the Attolab.

4.2   Results

In the first part of the work, all the efforts were focused on the beam pointing stabilization and in the second part on the power-locking. During the last step of the project work, after the system started to reply positively to the configuration, a long procedure of optimization has been performed. The fact that the process signal of the power and the two signals of the pointing are correlated, as exposed in section 3.3, a fine tuning of the feedback loops has been done in the final part of the work, in order to achieve good results for all the involved variables while both stabilization systems are running. Particular attention has been given to the frequency range of fluctuations. These oscillation components correspond to the mechanical vibrations and all those sources of laser noise described in chapter 2 that affect the position of the laser beam and the pulse energy.

---

*Helium neon

4.2.1   Beam Pointing Stabilization

The configuration of the hardware system and the development part of the LabVIEW™ software were the two first steps to get the project started. The system was initially mounted on a small optical bench, in a separate lab, where a testing optical setup with a chopped He–Ne laser and a focusing lens were mounted. The piezoelectric mirror was disposed in order to achieve suitable displacement ranges on the two axis. In fact the angular dynamics around the two axis of the piezoelectric mirror has to be converted in planar displacement†, with a proper focal length lens in order to reach a good span of fluctuation observations and corrections over the x- and y-directions. To increase the optical distance was decided to let the light go through multiple reflections on multiple mirrors, fixed on the small optical bench during the test phase of the work. Subsequently, all this was not needed since the piezoelectric mirror was disposed after the compressor, optically far enough for the desired control performance, using the focusing lens. All the hardware requirements were provided: the PSD was soldered on the signal processing circuit and the signals bundle cable shielded and connected between the signal processing circuit and the FPGA connector box. Several solutions were introduced to reduce the electromagnetic noise level, basically experimenting different connection types (differential mode, referenced single-ended mode), filtering and trying to ground in an advantageous way each device of the electronic setup. Typically, a lab is a source of electromagnetic noise in different frequency ranges, even at low frequencies observed in the dynamics of the present project. The initial inputs and tips for the FPGA software developed were kindly provided by Guillaume Genoud, who designed a similar pointing stabilization system for a different setup [?]. From that example, other different algorithms and from a fruitful assistance by National Instruments the software has been developed and tuned to better suit the hardware and the setup in the Attolab. Multiple useful features were included in the host program in order to allow the operator to have a wide control over the different parameters and to monitor all the different laser dynamics. The host program screen-shot is presented in appendix A. In order to collect the data points, the DMA feature included in the FPGA has been used. DMA is the acronym of Data Memory Access, and it exploits the FIFO structure (first-in-first-out) for the data transferring. In fact the process variables were "wired" to the corresponding DMA VI in the Virtual Instrument

---

†For the conversion it is simple to calculate the x- and y-displacement by $\Delta x = f \cdot \Delta\theta_x$ and $\Delta y = f \cdot \Delta\theta_y$, where $\Delta\theta_x$ and $\Delta\theta_y$ are the two angular misalignments.

program to get the data flux to work. In this way, from the host program, the operator can store data continuously to a file, in order to, *e.g.*, later analyze it in MATLAB. To use the DMA, two memory buffers have been created: one in memory on the FPGA device and one in memory of the host computer, and LabVIEW™ efficiently transfers data over the PCI bus from the FPGA VI to the host VI. The advantages in using this technology is the speed of the data transfer rate. The main quality of the FPGA is the fast sampling rate and in general, the speed of the operations (up to 40 MHz). The operative controller cycles programmed in the software run at 1 MHz, and the operator can decide and modify the value from the host program. The control process is however limited at 250 kHz due to the lower operative frequency of the A/D conversion. In this sense has to be pointed out that in the case of the measurements and during the tests, the situation has always been that of oversampling. Typically, both input and output repetition rate was set at 10 µs, corresponding to 100 times the frequency of the laser pulses. This has not been a problem but an advantageous strategy: since the oversampled signals come from a S&H circuit, the new points collected will be just affected by jittering, but over the entire millisecond between two consecutive pulses, the values would be roughly constants, and over the transitions, where a "step" is introduced to the system, the control output, sending a higher number of different data points to the output, keeps the actuator driver signals smoother.

Temporal characteristics

For the characteristics of the fluctuations, the laser dynamics has been measured for one hour with the control on and one hour with the control off. Most of the measurements have been taken after several hours of warm–up time of the laser system. This means that basically it is expected even without control to have a much higher stability compared to the first hours of operative time of the source. The DMA provides a storing sampling rate equal to the laser repetition rate, hence, the exact number of pulses detected are stored as vectors in the memory containing the three variables (x–, y–position and relative power), then the data flux is transferred from the FPGA to the computer and subsequently stored in a text file. Every cycle of the host program, the DMA memory buffer is emptied, so a proper memory size vs host repetition rate balance has to be found. In figure 4.3 on the next page the two series of data are represented in a 2–dimensional plot. This image gives an idea of how much the coupling surface of the light pulses with the hollow fiber

is reduced.

In this series of measurements, the beam fluctuations were approximately ± 30 μm (6.1 μm r.m.s.) in the vertical direction and ± 25 μm (4.1 μm r.m.s.) in the horizontal direction without the active control. These values already give an idea of a stable source, but as mentioned before, this series of data was taken late in the afternoon, after all day of operative time within which the optics can reach thermal equilibrium and less instabilities are introduced. With the control, the beam fluctuations were approximately ± 8 μm (1.2 μm r.m.s.) in the vertical direction and ± 8.5 μm (1.2 μm r.m.s.) in the horizontal direction. It should be remarked that the system, with a stronger choice of gain parameters in the controllers, is able to achieve even sub–μm r.m.s on both axis, but a compromise between the standard deviation of the spreading and the high frequency noise introduced due to the feedback loop has to be done, as it will be commented on later. For this reason soft gains are typically used over the working time, since the values obtained are good enough to increase the coupling stability of the hollow fiber and to optimize the broadening of the spectrum. Figures 4.4 and 4.5 show the time evolutions of the vertical and horizontal positions, respectively, over the hour of measurement with the control on and off. It is clear that the control system acts in the two temporal scales related to the different noise
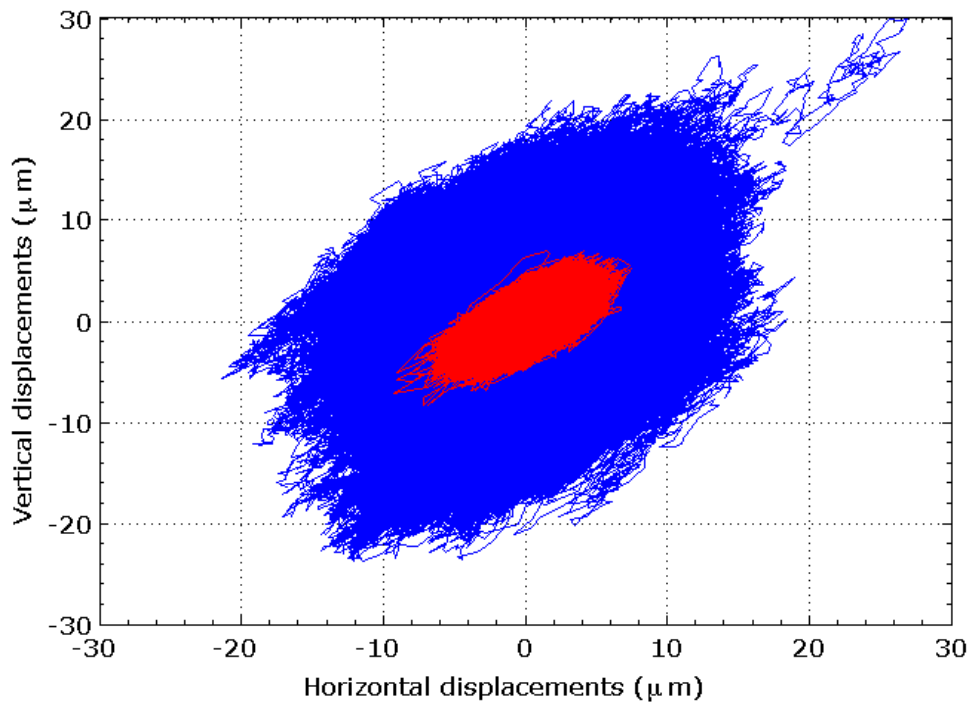

Figure 4.3: Shots collected over one hour. It can be noticed that the feedback control greatly reduces the drift of the laser beam in both directions.
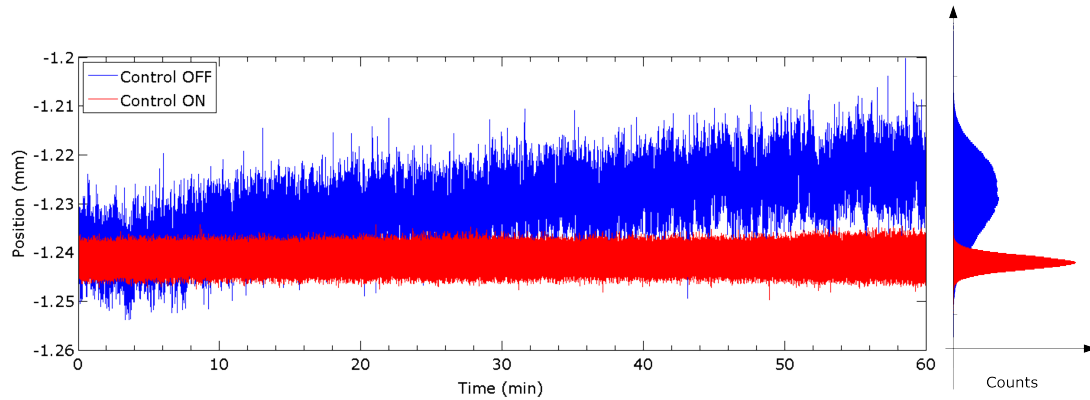
Figure 4.4: Vertical fluctuations over one hour with control on and off.

phenomena described in section 2.1. The position value has been kept on the ordinate to show the reference signal values (see section 3.4.1). The control action dearly reduces the short term drifts and it can be seen in the time series over the hour of data logging. The control action on the long term drift is more evident for the vertical fluctuations, in figure 4.4, where a slow displacement is evolving over the entire hour, and it is definitely evident looking how thinner became the spreading of the Gaussian plots, that are shown on the side of the graphs.

Fast Fourier Transform analysis

In order to visualize the frequency components of the fluctuations, and to be able to have an idea of the response of the system on them when the control action is activated, Fast Fourier Transforms of the signals have been computed in MATLAB for the two series of data acquired. The most important frequency range to be observed is between 0 and 100 Hz. In figure 4.6 it can be noticed that all the low frequency components are decreased by two to
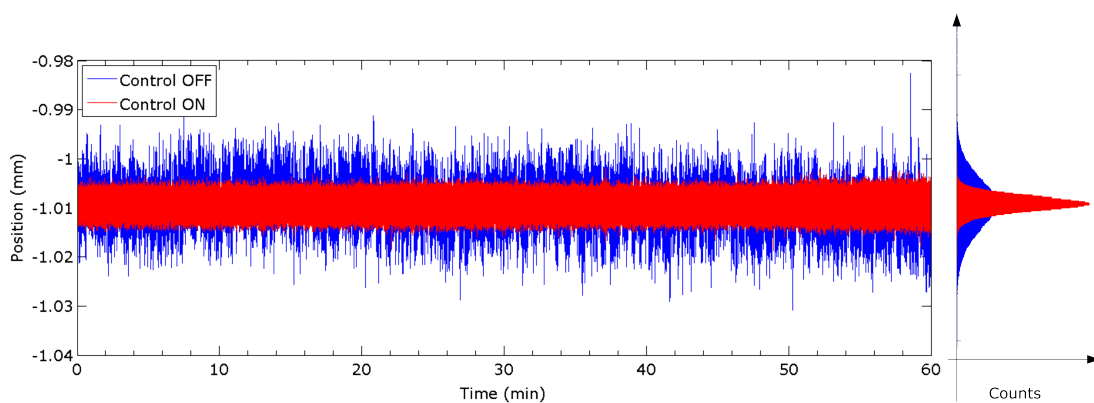

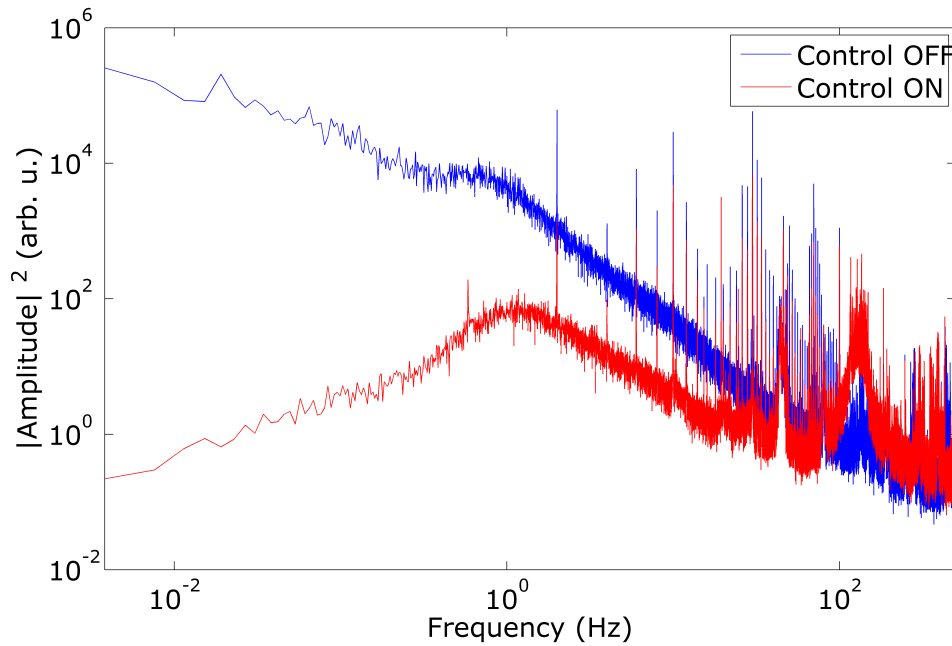Figure 4.5: Horizontal fluctuations over one hour with control on and off.

Figure 4.6: Spectral content of the vertical fluctuations signal.

three orders of magnitude, in correspondence of 0 to 10 Hz. These components are related to the slow drifting and they are smoothly corrected and almost completely eliminated. It can be noticed the broad peaks around 50 Hz, related to the alternate net current carrier frequency; further at 100 Hz compares also its second-harmonic. Those electrical noise source harmonics are not visibly reduced by the feedback loop since they are not of a
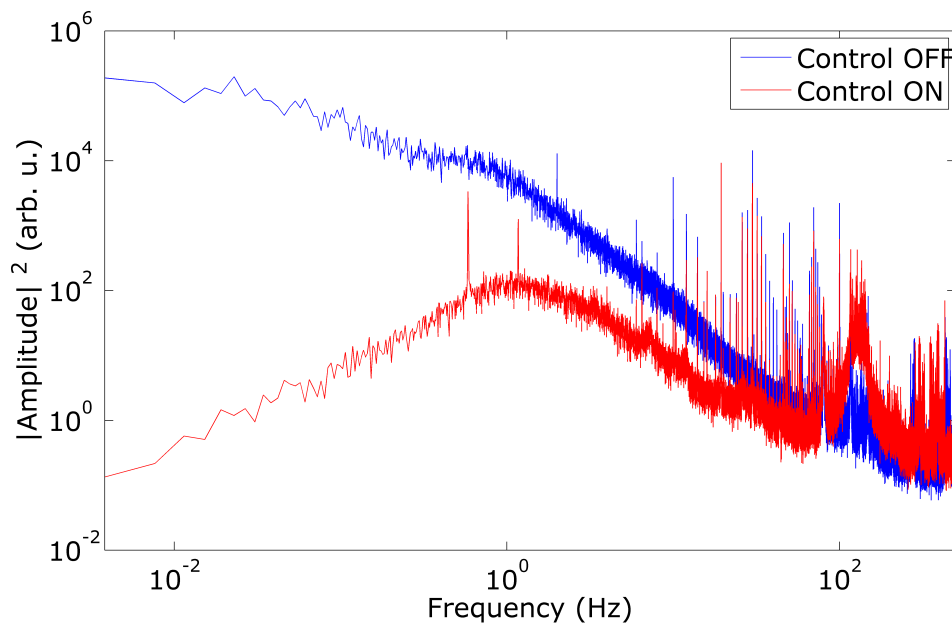

Figure 4.7: Spectral content of the horizontal fluctuations signal.

mechanical or thermal origin. Another consideration has to be done about the differences between the two axis spectra. In fact, as expected, the vertical fluctuations are greater in magnitude than the horizontal. This phenomena is explainable since more instabilities are introduced on the vertical direction; *e.g.*, the cryo-cooler vibrates in this direction. In general, the optical components (lenses, mirrors, irises, etc.) have more stability against vibrations along the horizontal directions, due to the position of the screws that keep tight those mounts to the optical benches. Essential aspect is the higher-frequencies noise introduced by the feedback loop when it is in action. In fact, additional high-frequency electrical harmonics are introduced due to the feedback action and the coupling of it with the process variables signals. This effect is exhibited for each variable.

4.2.2 Power locking

The work related to the power stabilization has been performed after the beam pointing stabilization. In fact, the relative power level signal of the PSD is used as process variable for the power-locking, that is correlated with the two position signals as it has been explained previously. With only one sensor and without the need of an additional power meter in the optical setup, both stabilization systems are implemented. Once the operator turns on the beam pointing stabilization control with the appropriate settings, the power locking can be started. In fact, a better intensity detection is performed by the PSD if the area of the beam drift is constrained. At this point the operator should introduce a small DC component to the driver of the acousto-optic modulator in order to have some of the laser power in the deflected beam, as explained before. This allows the process variable to oscillate around the set-point. Then the choice of the gain parameters and of the reference signal level permit the beginning of the power control.

Temporal characteristics

The relative power level data series has been plotted in the same way as the position data. The data was gathered for two hours: the first hour, first with the control off and then with the control on. As can be seen in figure 4.8, a great improvement has been reached. In the time domain, the power fluctuations around the average are reduced from 1.32% r.m.s. to 0.17% r.m.s., normalizing the deviation with the average level for each series. The jittering is then reduced to almost $1/8$ with respect the case without control.

In order to achieve this result, the PID action on the actuator driver has been pro-
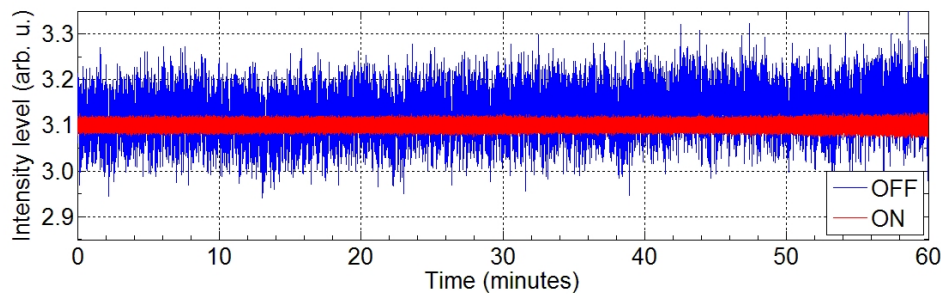
Figure 4.8: Shots representation collected over one hour. It can be noticed that the feedback control greatly decreases the fluctuations of the pulse energy.

portionated. The characteristics of the driver response to the control signal had to be tested in order to know the best driver output range within which the PID control signal should oscillate. In other measurements performed, even lower variation of the average power was recorded. In a series taken for half an hour, even values around 0.15% r.m.s. could be achieved. As was explained for the beam pointing stabilization, lower values are reachable by increasing the gain parameters of the control but then the higher–frequency noise introduced by the feedback loop is amplified. For this reason, even here, a trade off between the two effects is done.

Fast Fourier Transform analysis

The frequency component analysis reveals the magnitude of power fluctuations. In figure 4.9, the reader can see the impressive reduction of the harmonics up to 60 Hz, from almost 6 to circa 2 orders of magnitude. Even here, electromagnetic noise components are obviously present, and as anticipated before, those peaks do not change visibly between the control off and the control on because they are not controllable components. The operative bandwidth of the acousto–optic modulator is much higher than the piezoelectric mirror one; hence, a larger range of correctable frequencies is expected, but due to the correlation between the pointing process variables and the power relative level signal, the correctable frequency range remains the same for all of them (from 0 to 80 Hz circa).

4.3   Discussions and Outlook

The results achieved so far in the measurements and in the different tests executed reveal a great improvement due to the stabilization control device developed. The values obtained for the beam pointing fluctuations are comparable to the results obtained by the group of Akira Suda at RIKEN (using aggressives gains even better) [7], and much

better than the results obtained by a similar system using the same beam detection and signal processing in the attosecond laboratory in Milano. It should be mentioned that the initial idea, the sketch of the setup for the beam pointing stabilization, has been inspired by a continuous wave laser stabilization work, performed many years ago at the Physics Institution of the Heidelberg University [36]. With respect to the power locking, the result obtained is definitely satisfying, and the use of the acousto-optic modulator instead of a different modulator, like an electro-optic, was a good choice regarding electromagnetic noise emission. An electro-optic modulator works with much higher voltages, and in general emits more e.m. noise than others optical modulators. The result obtained is definitely better than the referenced work performed in J.R. Macdonald Laboratory in USA [5].

A limit of the system resides in the correlation between the position signals and the relative power signal. In fact, with a disassociation of those detections, it is probable that a better result can be achieved. But this solution would limit the optical setup choices, since it would need the introduction of an additional power meter in a certain point of the optical path. For the aim of the work, the achievements are in any cases appreciably improving the laser performances. The hollow fiber coupling is markedly improved by the spatial stability reached and mostly thanks to the pointing stabilization, the self-phase modulation effect is significantly better. Two spectrum of circa 20 minutes, respectively with the control on and off, has been recorded at the output of the hollow fiber to clearly show the better conducted SPM, due to its direct dependency on the intensity stability
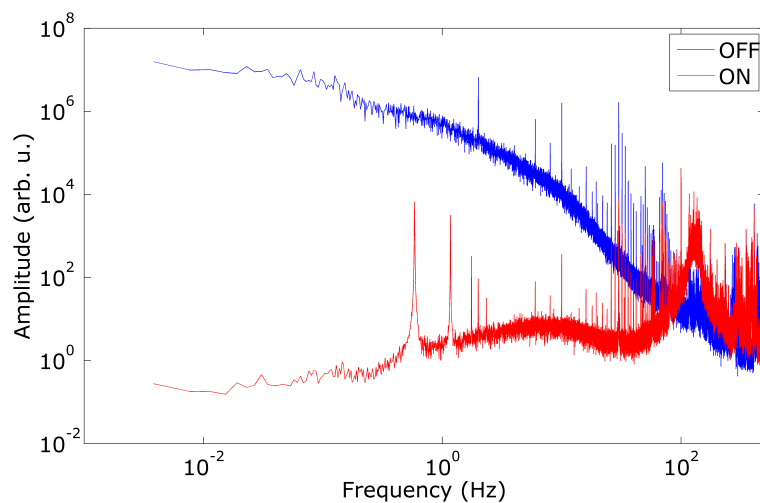

Figure 4.9: Spectral content of the power level signal.

and spatial displacements. The spectral shape is maintained much more stable over this time when the two controls are turned on, in fact in the other case can be noticed the change of the spectral profile over the time elapsed. It must be mentioned that even during this data sampling time the laser system was already well warmed up for several hours, hence, the contrast between the two spectra is not deeply definite.
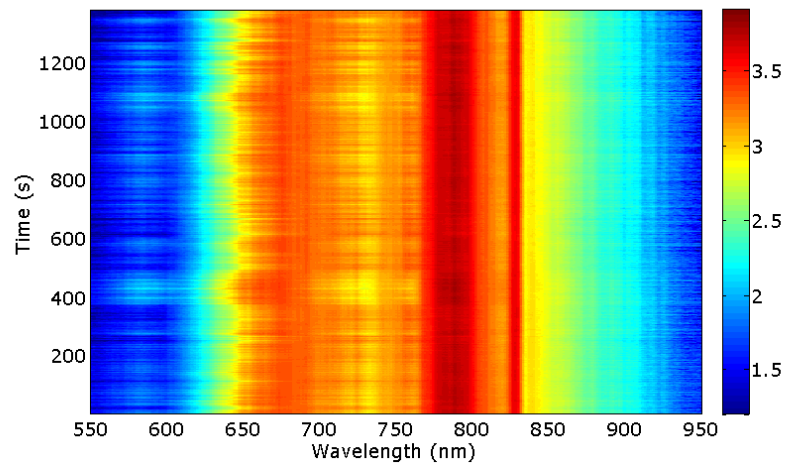
(a) *Control system OFF.*
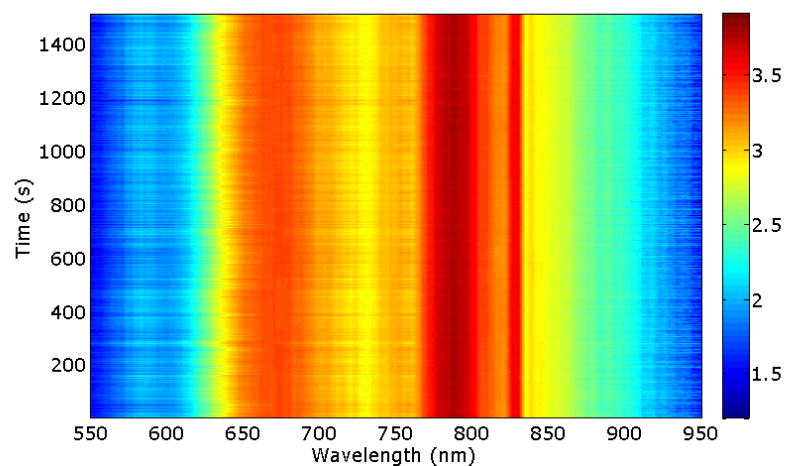
(b) *Control system ON.*

Figure 4.10: The Self-Phase Modulation in the hollow fiber is conducted with more stability and regularity all over the twenty minutes of spectrum recording, respectively with control off and on. It is clear that the broadening maintains its profile more constant over the time when the stabilization system is turned on.

A possible improvement of the entire system can be done in terms of frequency component corrections and a better noise rejection can be achieved with additional fine expedients. The use of a fast steering mirror instead of a piezoelectric mirror, *e.g.*, it would improve the bandwidth of the pointing stabilization controller. In addition, with an ex-

tension of the FPGA setup, it would be possible to integrate also the CEP control with the developed controllers into only one software on the same computer, in order to have an overview of all the parameters in one host program and simultaneously appreciate the benefit of the spatial and power controllers over the carrier-to-envelope phase offset locking.
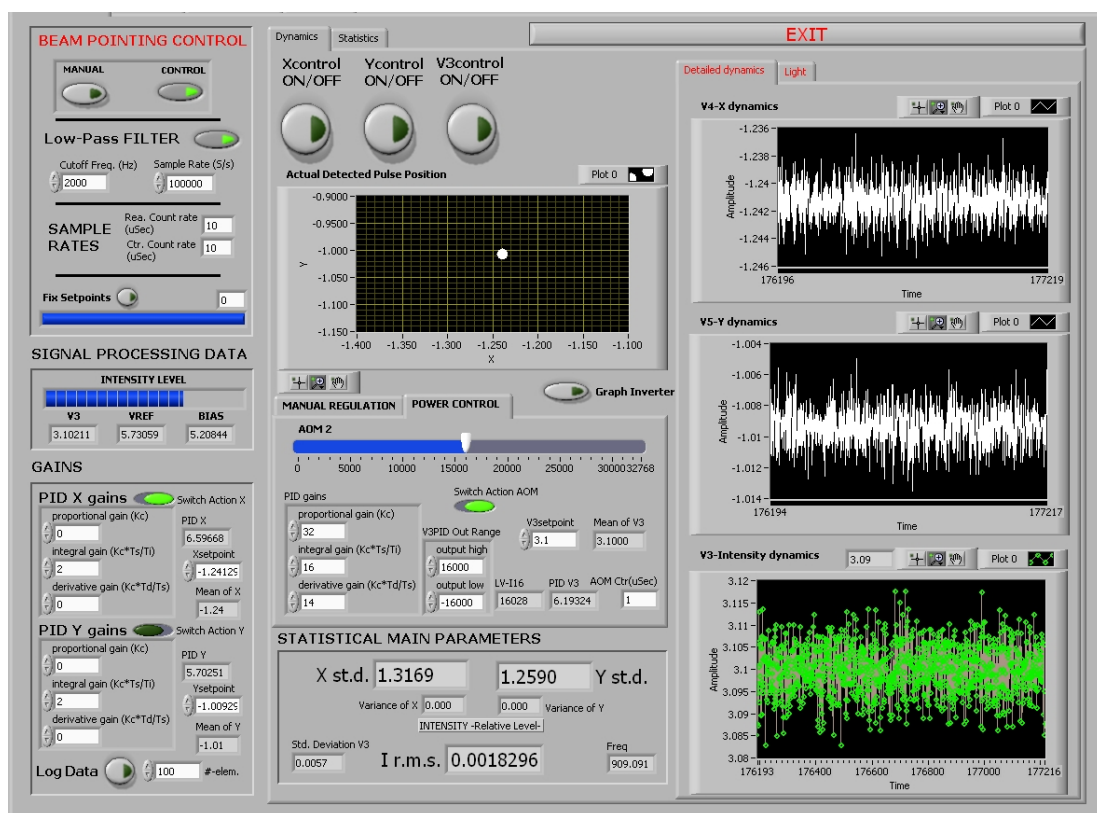
Appendix A

The host program

Figure A.1: Screen–shot of the host program while the stabilization of the laser is running.

Bibliography

[1] Mauro Nisoli. From Attoseconds to Controlled Dynamics: Recent Advances in XUV Sources. In *Frontiers in Optics (FiO)*. OSA Technical Digest (CD) (Optical Society of America, 2008).

[2] Rüdiger Paschotta. Noise in Laser Technology. Part 1: Intensity and Phase Noise. *Optik & Photonik*, No. 2:48–50, 2009.

[3] Rüdiger Paschotta. Noise in Laser Technology. Part 2: Fluctuations in Pulsed Lasers. *Optik & Photonik*, No. 3:45–47, 2009.

[4] Rüdiger Paschotta. Noise in Laser Technology. Part 3: Beam Pointing Fluctuations. *Optik & Photonik*, No. 1:55–57, 2010.

[5] He Wang, Chengquan Li, Jason Tackett, Hiroki Mashiko, Christopher M Nakamura, Eric Moon, and Zenghu Chang. Power locking of high-repetition-rate chirped pulse amplifiers. *Applied Physics B, Lasers and Optics*, 89(2-3):275–279, 2007.

[6] T Fordell, M Miranda, A Persson, and A L'Huillier. Carrier-envelope phase stabilization of a multi-millijoule, regenerative-amplifier-based chirped-pulse amplifier system. *Optics InfoBase*, 2009.

[7] Takuya Kanai, Akira Suda, S Bohman, M Kaku, S Yamaguchi, and K Midorikawa. Pointing stabilization of a high-repetition-rate high-power femtosecond laser for intense few-cycle pulse generation. *Applied Physics Letters*, 92, 2008.

[8] Sterling Backus, Charles G Durfee III, Margaret M Murnane, and Henry C Kapteyn. High Power Ultrafast Lasers. *Review of Scientific Instruments*, 69(3), 1998.

[9] Matteo Lucchini. Generazione di impulsi XUV ad attosecondi isolati mediante tecniche di campionamento temporale. Master thesis, Politecnico di Milano, Dipartimento di Fisica.

[10] Marko Swoboda. *Attosecond Wave Packet Metrology*. Ph.d. thesis, Lund University, Faculty of Engineering, 2010.

[11] M V Ammosov, N B Delone, and V P Krainov. Tunnel ionization of complex atoms and of atomic ions in an alternating electromagnetic field. *Soviet Physics - JETP*, 64(6):1191–1194, 1986.

[12] E Mansten, J.˜M. Dahlström, P Johnsson, M Swoboda, A L'Huillier, and J Mauritsson. Spectral shaping of attosecond pulses using two-colour laser fields. *New Journal of Physics*, 10(8):083041−+, 2008.

[13] Claude Rullière. *Femtosecond Laser Pulses Principles and Experiments*. Springer, ii edition, 2005.

[14] P M Paul, E S Toma, P Breger, G Mullot, F Augé, Ph. Balcou, H G Muller, and P Agostini. Observation of a Train of Attosecond Pulses from High Harmonic Generation. *SCIENCE*, 292:1689–1692, 2001.

[15] E Gustafsson, T Ruchon, M Swoboda, T Remetter, E Pourtal, R López-Martens, Ph. Balcou, and A L'Huillier. Broadband attosecond pulse shaping. *Opt. Lett.*, 32(11):1353–1355, 2007.

[16] Phillip V Mitchell. Fast Steering Mirror Technology: Active Beam Stabilization. *Application Note: Opto-mechanics, Technology Development, Newport Corporation*, DS-01012, 2009.

[17] R Paschotta. Encyclopedia of Laser Physics and Technology. \url{http://www.rp-photonics.com/encyclopedia.html}.

[18] Jean-Claude Diels and Wolfgang Rudolph. *Ultrashort Laser Pulse Phenomena*. Optical Engineering. Elsevier, Academic Press, second edi edition, 2006.

[19] Ferenc Krausz and Misha Ivanov. Attosecond physics. *Reviews of Modern Physics*, 81:163–234, 2009.

[20] Donna Strickland and Gerard Mourou. Compression of Amplified Chirped Optical pulses. *Optics Communications*, 56(3):219–221, 1985.

[21] Orazio Svelto. *Priciples of Lasers*. Springer, v edition, 2010.

[22] Andrew M Weiner. *Ultrafast Optics*. WILEY, 2009.

[23] Michael Perry. Multilayer Dielectric Gratings. *Science & Technology Review*, pages 24–33, 2005.

[24] Mauro Nisoli, Sandro De Silvestri, and Orazio Svelto. Generation of high energy 10 fs pulses by a new pulse compression technique. *Applied Physics Letters*, 68(20):2793–2795, 1996.

[25] Yu Oishi, Akira Suda, Katsumi Midorikawa, and Fumihiko Kannari. Sub-10 fs, multimillijoule laser system. *Review of Scientific Instruments*, 76(9):93114, 2005.

[26] Govind P Agrawal. *Nonlinear Fiber Optics*. Academic Press, iv edition, 2007.

[27] E A J Marcatili and R A Shmeltzer. Hollow Metallic and Dielectric Wave-guides for Long Distance Optical Transmission and Lasers. *The Bell System Technical Journal*, pages 1783–1809, 1964.

[28] Eisuke Haraguchi, Kanako Sato, Takashi Tanigawa, Mikio Yamashita, and Taro Sekikawa. Efficient Compression of Carrier-Envelope Phase-Locked Laser Pulses to 5.2 fs Using an Al-Coated Hollow Fiber. *Japanese Journal of Applied Physics*, 48:3,10211–10213, 2009.

[29] Robert W Boyd. *Nonlinear optics*. Academic Press, third edi edition, 2007.

[30] Steven T Cundiff. Phase stabilization of ultrashort optical pulses. *Journal of Physics D: Applied Physics*, 35:R43–R59, 2002.

[31] Hamamatsu Photonics K.K. Characteristic and use of Position Sensitive Detectors, Application Note.

[32] Hamamatsu. *Signal Processing Circuit Manual C7563*, k32-b60009 edition.

[33] Bèla G. Lipták. *Instrument Engineers' Handbook: Process control and optimization*, volume 2 of *Instrument Engineers' Handbook*. CRC Press, 2005. Chapter 2.

[34] You Wu, Doug French, and Igor Jovanovic. Passive beam pointing stabilization. *Optics letters*, 35(2):250–252, 2010.

[35] B E A Saleh and M C Teich. *Fundamentals of Photonics*. Wiley, ii edition, 2007.

[36] S Grafström, U Harbarth, J Kowalski, R Neumann, and S Noehte. Fast laser beam position control with submicroradian precision. *Optics Communications*, 65(2):121–126, 1988.